

# Solitons and Their Ghosts in $\mathcal{PT}$ -Symmetric Systems with Defocusing Nonlinearities

V. Achilleos, P.G. Kevrekidis, D.J. Frantzeskakis, and R. Carretero-González

**Abstract** We examine a prototypical nonlinear Schrödinger model bearing a defocusing nonlinearity and Parity-Time ( $\mathcal{PT}$ ) symmetry. For such a model, the solutions can be identified numerically and characterized in the perturbative limit of small gain/loss. There we find two fundamental phenomena. First, the dark solitons that persist in the presence of the  $\mathcal{PT}$ -symmetric potential are destabilized via a symmetry breaking (pitchfork) bifurcation. Second, the ground state and the dark soliton die hand-in-hand in a saddle-center bifurcation (a nonlinear analogue of the  $\mathcal{PT}$ -phase transition) at a second critical value of the gain/loss parameter. The daughter states arising from the pitchfork are identified as “ghost states”, which are not exact solutions of the original system, yet they play a critical role in the system’s dynamics. A similar phenomenology is also pairwise identified for higher excited states, with e.g. the two-soliton structure bearing similar characteristics to the zero-soliton one, and the three-soliton state having the same pitchfork destabilization mechanism and saddle-center collision (in this case with the two-soliton) as the one-dark soliton. All of the above notions are generalized in two-dimensional settings for vortices, where the topological charge enforces the destabilization of a two-vortex state and the collision of a no-vortex state with a two-vortex one, of a

---

V. Achilleos · D.J. Frantzeskakis  
Department of Physics, University of Athens, Panepistimiopolis, Zografos, Athens 157 84,  
Greece  
e-mail: [vassosnbi@gmail.com](mailto:vassosnbi@gmail.com); [dfrantz@phys.uoa.gr](mailto:dfrantz@phys.uoa.gr)

P.G. Kevrekidis  
Department of Mathematics and Statistics, University of Massachusetts, Amherst,  
MA 01003-4515, USA  
e-mail: [kevrekid@math.umass.edu](mailto:kevrekid@math.umass.edu)

R. Carretero-González (✉)  
Nonlinear Dynamical Systems Group, Department of Mathematics and Statistics, Computational  
Science Research Center, San Diego State University, San Diego, CA 92182-7720, USA  
e-mail: [rcarretero@mail.sdsu.sdsu](mailto:rcarretero@mail.sdsu.sdsu); <http://nlds.sdsu.edu/>

one-vortex state with a three-vortex one, and so on. The dynamical manifestation of the instabilities mentioned above is examined through direct numerical simulations.

## 1 Introduction

Over the past decade, and since they were originally proposed by Bender and co-workers [1, 2], systems characterized by  $\mathcal{PT}$ -symmetric Hamiltonians have become a subject of intense research efforts. The interest in these systems arises from their fundamental property to exhibit real spectra, while non-Hermitian, thus providing an intriguing alternative to standard Hermitian quantum mechanics. In the case of a standard Schrödinger-type Hamiltonian, with a generally complex potential  $U$ , the  $\mathcal{PT}$  symmetry dictates that the potential satisfies the condition  $U(x) = U^*(-x)$ , where  $(\cdot)^*$  stands for complex conjugation.

Optical systems appear to be ideal settings for the realization of  $\mathcal{PT}$ -symmetry; this was first proposed in Ref. [3], for an optical slab waveguide with a gain region and a loss region. We note that studies in optical systems with gain and loss were already performed as early as in 1992, in the setting of a twin core nonlinear coupler [4] (of course, at that time,  $\mathcal{PT}$ -symmetry had not been introduced). Nevertheless, an important development in the study of such models was the work of Refs. [5, 6], where both theoretical and experimental studies on  $\mathcal{PT}$ -symmetric optical systems were reported. In the optics context, a key element that comes into play in the physics of such systems is nonlinearity. Therefore, the considerations of Refs. [5, 6] extended from bright and gap solitons to linear (Floquet-Bloch) eigenmodes in periodic potentials, examining how these coherent structures are affected by the genuinely complex, yet  $\mathcal{PT}$ -symmetric potentials. More recently, experimental results were reported both in nonlinear optical systems [7, 8] and electronic analogs thereof [9]. These, in turn, have triggered a wide range of theoretical studies on nonlinear lattices with either linear [10–23] or nonlinear [24–26]  $\mathcal{PT}$ -symmetric potentials and, more recently, on harmonic  $\mathcal{PT}$ -symmetric potentials [27].

In the above works, numerous features extending from bright solitons to defect modes, and from gap solitons to  $\mathcal{PT}$ -lattices have been examined. Nevertheless, the consideration of defocusing nonlinearities, and especially of dark solitons has received limited attention; see, e.g., Refs. [27–29]. Another theme that despite its considerable relevance has also been considered only by a few works is that of higher dimensionality. For the latter, the focusing nonlinearity case [5, 6] has been examined, especially so in the context of lattice potentials. Our aim herein is to provide a systematic analysis of  $\mathcal{PT}$ -symmetric Hamiltonians exhibiting defocusing nonlinearities. In particular, and building on the earlier work of Ref. [29], we give a detailed account of the existence, stability and dynamical properties of the ground state and first few excited states namely dark solitary waves and vortex two-dimensional generalizations thereof. This is done specifically in a prototypical context of the nonlinear Schrödinger type which can, in principle, be relevant both in the case of Bose-Einstein condensates [30], as well as in that of nonlinear

optics [31]; see the detailed justification of the real and imaginary parts of the potential below.

Our main findings and their presentation are structured as follows.

- In Sect. 2, we put forth the general model and consider its physical relevance.
- In Sects. 3 and 4, we turn to generic potentials and the features of their ground and excited states in one-dimension. We find that odd excited states (1-soliton, 3-soliton, 5-soliton, etc.) become subject to a symmetry breaking bifurcation. The pitchfork nature of this event is rationalized through the introduction of so-called ghost states which arise from it and which are exact solutions of the steady state but remarkably not ones such of the original full problem. Nevertheless, direct numerical simulations clearly identify the ensuing symmetry breaking and manifest the dynamical role of the ghost waveforms. One more important feature identified is the nonlinear analogue of the  $\mathcal{PT}$ -phase transition. In particular, between the (unstable, for sufficiently strong gain/loss) saddles of the odd excited states and the centers of the even states (ground state, 2-soliton, 4-soliton, etc.), there is a pairwise collision and disappearance (blue-sky or saddle-center) event. This is strongly reminiscent of the corresponding transition of linear eigenstates of the Hamiltonian originally reported in Ref [1]. Direct numerical simulations are employed in order to identify the evolution dynamics of the unstable solitary wave states and also their dynamics past the  $\mathcal{PT}$ -phase transition point in Sect. 5. The ghost states are then examined separately in their own right in Sect. 6.
- In Sect. 7, we illustrate how each of the above parts of the picture is generalized in the two-dimensional variant of the relevant model. There, the charge of the vortex states imposes topological constraints enforcing that the ground state may only collide and disappear (in a nonlinear  $\mathcal{PT}$ -phase transition) with the two-vortex (of opposite charge, namely dipole) state. Similarly, the single vortex and triple (of alternating charge) suffer a saddle-center bifurcation and so on. Prior to these events, a destabilization of the two-vortex (and three-vortex etc.) states arises through a pitchfork event creating ghost vortex states. The latter are illustrated dynamically as well and the structural analogies of the one- and two-dimensional settings are explored both in the statics and in the dynamics. Lastly, Sect. 8 presents a brief summary of our conclusions and a number of potential directions for future study.

## 2 The Model and Some Analytical Insights

Our model, which can be equally applied to a variety of one-dimensional and even higher dimensional systems is a nonlinear Schrödinger (NLS) equation incorporating a complex potential. This equation, which finds applications in the contexts of nonlinear optics [31] and in the physics of atomic Bose-Einstein condensates [30], is expressed in the following dimensionless form:

$$i \partial_t u = -\frac{1}{2} \partial_x^2 u + |u|^2 u + [V(x) + iW(x)]u, \quad (1)$$

where  $u$  is a complex field, denoting the electric field envelope in the context of optics (or the macroscopic wavefunction in BECs),  $t$  denotes the propagation distance (or time in BECs),  $x$  is the transverse direction, while  $V(x)$  and  $W(x)$  denote, respectively, the real and imaginary parts of the external potential. For a  $\mathcal{PT}$ -symmetric Hamiltonian,  $V(x)$  and  $W(x)$  must be, respectively, an even and an odd function of  $x$ , namely:

$$\begin{cases} V(x) = V(-x), \\ W(x) = -W(-x). \end{cases} \quad (2)$$

Physically speaking, in the context of optics,  $V(x)$  and  $W(x)$  represent, respectively, the spatial profiles of the real and imaginary parts of the refractive index. The above requirements for the parities of  $V(x)$  and  $W(x)$  can be met in a case where  $V(x)$  has, e.g., a parabolic profile and  $W(x)$  has an anti-symmetric profile (amounting to equal and opposite gain and loss), as in the experiment of Ref. [8]. In the context of BECs,  $V(x)$  represents the external trap (necessary to confine the atoms [30]) and  $W(x)$  accounts for a mechanism for injecting and removing particles in equal rates. The requirement for the parity of the trap  $V(x)$  can easily be met in the case of e.g., the usual parabolic potential (representing a magnetic trap) or a double-well potential (representing a combination of a magnetic trap with a suitable optical lattice) [30]. On the other hand,  $W(x)$  is odd if an equal number of atoms is injected and removed from spatial regions symmetrically located around the trap center. Such a setting was originally proposed in Ref. [32] for a BEC confined in a double-well potential, but no physical mechanism for such a realization was offered (notice that although a localized particle loss can be implemented by an electron beam [33], the realization of a localized gain has not been proposed so far). Furthermore, passive parity-time symmetric analogs of the double well system (featuring only loss in one well and no gain) have also been proposed in the context of the so-called open Bose-Hubbard dimer [34]; see also Refs. [13, 14]. More recently, a very large volume of activity has focused on such double-well potentials in a balanced gain-loss (i.e.,  $\mathcal{PT}$ -symmetric) form; see, for instance, Refs. [35–38]. In such contexts, some of the notions presented below, such as the ghost states and their emergence from suitable bifurcations and dynamical relevance, can be both numerically manifested, as well as analytically demonstrated.

We seek standing wave solutions of Eq. (1) in the form  $u = \rho(x) \exp[i\phi(x) - i\mu t]$ , where the real functions  $\rho(x)$  and  $\phi(x)$ , and the real constant  $\mu$  represent, respectively, the amplitude, phase and propagation constant (in optics) or chemical potential (in BECs). Substituting this ansatz into Eq. (1), and separating real and imaginary parts, we obtain the following coupled boundary-value problems (BVPs):

$$\mu\rho = -\frac{1}{2}(\rho_{xx} - \rho\phi_x^2) + \rho^3 + V(x)\rho \quad (3)$$

$$2W(x)\rho^2 = (\rho^2\phi_x)_x, \quad (4)$$

where subscripts denote partial derivatives. For generic potentials  $V(x)$  and  $W(x)$ , the relevant  $\mathcal{PT}$ -symmetric problem involves solving the BVPs for  $\rho$  and  $\phi$ . Notice the critical role of the imaginary part of the potential in dictating the phase profile  $\phi(x)$ . We will chiefly focus on the case of a real parabolic potential,

$$V(x) = \frac{1}{2}\Omega^2x^2, \quad (5)$$

with strength  $\Omega$ , modeling the transverse distribution of the refractive index (or the external trap in BECs) as mentioned above, while the imaginary part  $W(x)$  will be considered to be an odd, localized function of space, of spatial width  $\ll \Omega^{-1}$ . Such a form of  $W(x)$  is consistent with the experimental work of Ref. [8] in a nonlinear optics setup and could be relevant to an effective description of atom loss/gain mechanisms in trapped BECs. Our analysis will be general (independent of the particular form of  $W(x)$ ), and we will showcase our results in the case of the following prototypical example:

$$W(x) = \varepsilon x \exp(-x^2/2), \quad (6)$$

where  $\varepsilon$  is a parameter setting the magnitude of the imaginary potential (a generalization of this model in two-dimensions will be studied in Sect. 7). We should mention that our analytical approximations (see below) can also be applied for other choices, e.g., when  $W(x)$  takes the form  $W(x) = \varepsilon \operatorname{sech}^2(x) \tanh(x)$ ; in such cases, we have checked that our results remain qualitatively similar to the ones that we will present below.

We conclude this section by noting the following. Below we will study the ground state and excited states of the system (in the form of dark solitons). In that regard, it is relevant to consider the evolution of the physically relevant quantity  $N = \int |u|^2 dx$ , which represents power in optics or number of atoms in BECs. Employing Eq. (1), it is straightforward to find that  $dN/dt$  is governed by the equation:

$$\frac{dN}{dt} = 2 \int_{-\infty}^{+\infty} |u|^2 W(x) dx. \quad (7)$$

Thus, since  $W(x)$  is odd, it is obvious that the power is conserved as long as the square modulus profile of the ground state or of the excited states remains even. Below, we will show that for genuinely stationary states this is the case, indeed and we will examine the important consequences of Eq. (7) on the bifurcations and dynamics of the system at hand.

### 3 Ground State and Single Dark Soliton

#### 3.1 Ground State

First, we will study the existence and stability of the most fundamental state of the system, namely the ground state. The latter is sought as a stationary solution of Eq. (1) in the form  $u = u_b(x) \exp(-i\mu t)$  (where  $\mu$  is the propagation constant or the chemical potential in BECs), with the background field  $u_b$  obeying the equation:

$$-\frac{1}{2}\partial_x^2 u_b + |u_b|^2 u_b + [V(x) + iW(x)]u_b - \mu u_b = 0. \quad (8)$$

For a sufficiently small imaginary potential,  $W(x) = \varepsilon \tilde{W}(x)$  (with  $\max\{|\tilde{W}(x)|\} = O(1)$ ), where  $\varepsilon \ll 1$ , and when the inverse width  $\Omega^{-1}$  of  $V(x)$  is sufficiently large so that  $\Omega \sim \varepsilon$ , we may find an approximate solution of Eq. (1) in the Thomas-Fermi (TF) limit [30, 39]. This solution is of the form:

$$u_b(x) = [\sqrt{\mu} + f(x)] \exp[i\phi(x)], \quad (9)$$

where the amplitude and phase  $f(x)$  and  $\phi(x)$  (considered to be small, of order  $\varepsilon^2$  and  $\varepsilon$ , respectively) are given by:

$$f(x) = -\frac{1}{2\sqrt{\mu}} (V(x) + 2W^2(x)), \quad (10)$$

$$\phi(x) = 2 \int \mathcal{W}(x) dx. \quad (11)$$

where  $\mathcal{W}(x) = \int W(x) dx$ , and we have neglected terms of order  $O(\varepsilon^3)$  (notice that the integral in Eq. (11) is an indefinite one). Contrary to the conservative case ( $\varepsilon = 0$ ) [30], this TF background is characterized by a density dip located at the center,  $x = 0$ , and a nontrivial (tanh-shaped) phase distribution; similar features of the ground state were also reported in Ref. [27] (but for an extended gain/loss potential). The density and phase profiles are shown in Fig. 1, where the analytical result (dashed lines) is compared with the numerical one (solid lines); the agreement between the two is excellent. Note that we have checked that the above solution stays close to the numerically found ground state of the system up to the order  $\mathcal{O}(\varepsilon^2)$  [29].

The evolution of the density of the TF background indicates that the ground state is stable (see more details in the analysis below). Importantly, a linear stability—Bogoliubov-de Gennes (BdG)—analysis (see, e.g., Ref. [39]) justifies the above argument, showing that the background  $u_b(x)$  is indeed stable against small perturbations.

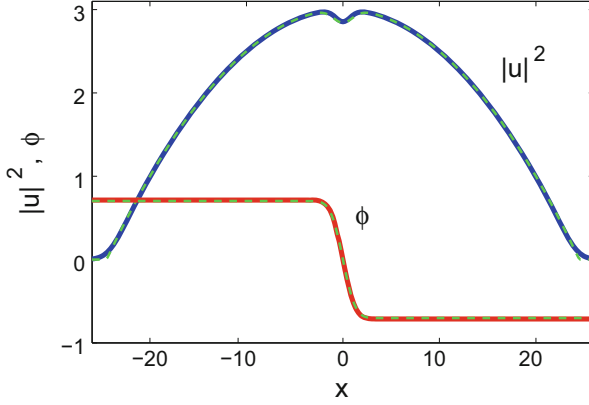


**Fig. 1** The density (solid (blue) line) and phase (solid (red) line) of the numerically obtained TF background compared to the prediction of Eq. (11) (dashed (green) lines). The parameters values are:  $\mu = 3$ ,  $\Omega = 0.1$  and  $\varepsilon = 0.3$

### 3.2 Single Dark Soliton

Apart from the ground state, excited states of the system—in the form of stationary dark solitons—can also be found numerically, by means of a fixed point algorithm (Newton’s method). A pertinent example of the form of a single dark soliton is shown in the top panel of Fig. 2.

To analyze the dynamics of such a single dark soliton, described by function  $v(x, t)$ , on top of the TF background, we introduce the product ansatz:  $u = u_b(x)v(x, t)$  into Eq. (1) (i.e., we decompose the solution into a soliton and its background). Then, we employ the expressions (9)–(11) for  $u_b$ , and derive the following equation for  $v(x, t)$ :

$$i \partial_t v + \frac{1}{2} \partial_x^2 v - |u_b|^2 (|v|^2 - 1) v = -\partial_x \ln(u_b) \partial_x v, \quad (12)$$

which is derived upon dividing with the TF background  $u_b(x)$  assuming that  $|x| \leq R = \sqrt{2\mu}/\Omega$  (the so-called TF radius). We then simplify the resulting equation for  $v(x, t)$  by keeping only leading-order terms, up to order  $\mathcal{O}(\varepsilon^2)$  in  $u_b$  (recall that the function  $f(x)$  is of order  $\mathcal{O}(\varepsilon^2)$ ). To this end, using the scale transformations  $t \rightarrow \mu t$  and  $x \rightarrow \sqrt{\mu}x$ , we obtain the following perturbed NLS equation:

$$i \partial_t v + \frac{1}{2} \partial_x^2 v + v(1 - |v|^2) = P(v), \quad (13)$$

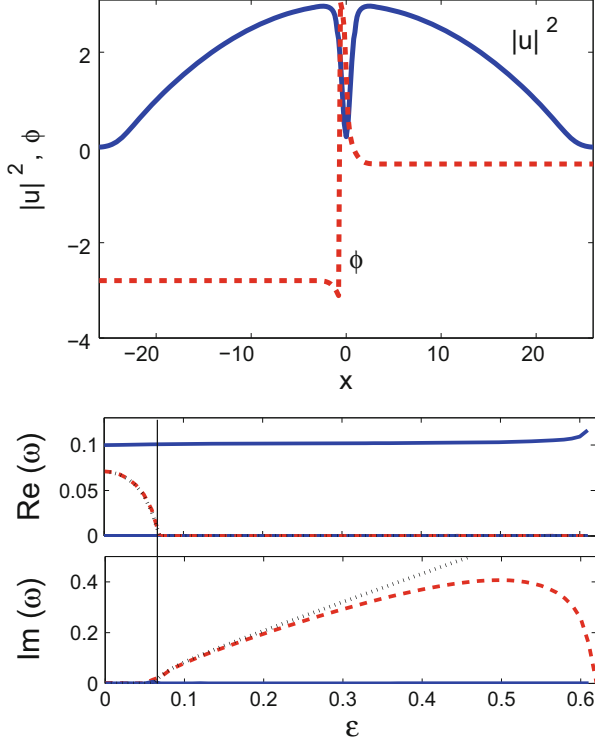


**Fig. 2** *Top panel:* The density (solid (blue) line) and phase (dashed (red) line) of the first excited (single dark soliton) state for  $\varepsilon = 0.3$ . *Middle and bottom panels:* The linear spectrum of the single dark soliton branch: *middle (bottom) panel* shows the real (imaginary) part of the lowest eigenfrequencies  $\omega$ , with respect to the amplitude  $\varepsilon$ . The dashed (red) line depicts the mode  $\omega_\alpha$ , which coincides with the anomalous mode for  $\varepsilon = 0$ ; while the dotted (black) line is the analytical result of Eq. (21). The vertical line shows the point  $\varepsilon_{\text{cr}}^{(1)}$ , where the bifurcation emerges. The parameters used are:  $\mu = 3$  and  $\Omega = 0.1$

where the functional perturbation  $P(v)$  is given by

$$P(v) = \mu^{-2} \left[ (1 - |v|^2)v (V + 2W^2) + v_x \left( \frac{1}{2} V_x - 2(W - i)W \right) \right]. \quad (14)$$

Applying the perturbation theory for dark solitons devised in Ref. [40] (see also Ref. [39]), we seek a solution of Eq. (13) in the form of the dark soliton of the unperturbed system ( $P(v) = 0$ ):

$$v(x, t) = \cos \varphi(t) \tanh \xi + i \sin \varphi(t). \quad (15)$$

Here,  $\xi \equiv \cos \varphi(t) [x - x_0(t)]$ , while the unknown, slowly-varying functions  $\varphi(t)$  and  $x_0(t)$  represent, respectively, the phase ( $|\varphi| \leq \pi/2$ ) and center of the soliton,

while  $dx_0/dt = \sin \varphi$  accounts for the soliton velocity. In the framework of the adiabatic approximation, the perturbation-induced evolution equations for  $x_0(t)$  and  $\varphi(t)$  read:

$$\frac{dx_0}{dt} \approx \varphi(t), \quad (16)$$

$$\frac{d\varphi}{dt} \approx -\frac{1}{2} \partial_x V(x) - \int \operatorname{sech}^4(\xi) [\tanh(\xi) \mathcal{W}^2(x) + W(x) \mathcal{W}(x)] dx, \quad (17)$$

where we have assumed almost black solitons with sufficiently small phase angles  $\phi(t)$ , such that  $\sin \phi \approx \phi$ ; such an assumption is relevant for solitons moving close to the trap center ( $x \approx 0$ ), an assumption already used in the derivation of Eq. (17)—see more details and discussion in Ref. [39]. Thus, generally, for a given imaginary potential  $W(x)$ , and by calculating the above integral, we can derive an equation of motion for the dark soliton center  $x_0$  in the form:

$$\frac{d^2 x_0}{dt^2} = -\frac{\partial V_{\text{eff}}}{\partial x_0}, \quad (18)$$

where  $V_{\text{eff}}$ , is the effective potential felt by the single soliton.

In the case where the imaginary part of the potential takes the form of Eq. (6), we numerically calculate the integral in Eq. (17) and find that the effective potential can be approximated as:

$$V_{\text{eff}}(x_0) = \frac{1}{2} \left( \frac{\Omega}{\sqrt{2}} \right)^2 x_0^2 + \frac{\varepsilon^2 c_1}{4c_2} \operatorname{sech}^4(c_2 x_0). \quad (19)$$

where  $c_1 \approx 1.9$  and  $c_2 \approx 0.6$ . Notice that the effective potential contains essentially two contributions, the first from the external parabolic trap (as is the case in the context of BECs [30, 39, 41]), and the second from the presence of the imaginary potential  $W(x)$ .

To examine the stability of the equilibrium at  $x_0 = 0$  (i.e., the stability of a quiescent black soliton located at the trap center), we Taylor expand the effective potential of Eq. (19) around  $x_0 = 0$ , and find—to leading order—the following equation of motion for the soliton center [29]:

$$\frac{d^2 x_0}{dt^2} = -\omega_{\text{osc}}^2 x_0, \quad (20)$$

$$\omega_{\text{osc}}^2 \approx \left( \frac{\Omega}{\sqrt{2}} \right)^2 - 1.14 \varepsilon^2. \quad (21)$$

Equation (21) implies that if the amplitude  $\varepsilon$  of  $W(x)$  is less than a critical value  $\varepsilon_{\text{cr}}^{(1)} \approx 0.66 \Omega$ , the soliton performs oscillations in the complex potential with frequency  $\omega_{\text{osc}}$ ; on the other hand, if  $\varepsilon > \varepsilon_{\text{cr}}^{(1)}$  the soliton becomes unstable. In fact,

the prediction has the quintessential characteristics of a pitchfork bifurcation. For  $\varepsilon < \varepsilon_{\text{cr}}^{(1)}$ , the relevant potential is monostable at  $x_0 = 0$ , while beyond the critical point, two symmetric minima arise (in this effective potential picture) and the center position becomes the saddle point that separates them.

The above prediction about the change of stability of the critical point at  $x_0 = 0$  has been confirmed numerically, both by means of direct simulations and by employing a BdG analysis. The latter reveals that the considered stationary dark soliton is characterized by a mode  $\omega_\alpha$  (initially coinciding with the anomalous mode [39, 41] for  $\varepsilon = 0$ ), which is real for  $\varepsilon < \varepsilon_{\text{cr}}^{(1)}$  (in this case,  $\omega_\alpha = \omega_{\text{osc}}$ ), and it becomes imaginary for  $\varepsilon > \varepsilon_{\text{cr}}^{(1)}$ , thus signaling the onset of the spontaneous symmetry breaking (SSB) instability of the dark soliton (which should be expected to displace the soliton from the trap center).

The dependence of  $\omega_\alpha$  on the amplitude  $\varepsilon$  of the imaginary potential  $W(x)$ , as found by the BdG analysis, is illustrated in the middle and bottom panels of Fig. 2. The mode, corresponding to the oscillatory motion of the dark soliton, is the first non-zero mode in the real part of the spectrum, indicated with a dashed (red) line—cf. middle panel of Fig. 2. We observe that it initially moves towards the spectral plane origin, and past the critical point,  $\varepsilon_{\text{cr}}^{(1)}$  (cf. vertical line),  $\omega_\alpha$  becomes imaginary, and thus the soliton becomes unstable. The corresponding pair of imaginary eigenfrequencies is shown in the bottom panel of Fig. 2. The solid (black) line in both panels, shows the analytical result of Eq. (21). An excellent agreement between the analytical prediction and the BdG numerical result is observed even beyond the SSB bifurcation point, while for larger values of the parameter  $\varepsilon$ , perturbation theory fails and, as expected, the agreement becomes worse.

Importantly, for large values of the parameter  $\varepsilon$ , the imaginary eigenfrequencies start moving towards the spectral plane origin and collide with it at a second critical point,  $\varepsilon_{\text{cr}}^{(2)}$ , after which the branch is terminated. To better understand how the branch ceases to exist, we first observe (bottom panel of Fig. 1) that the density profile of the soliton becomes increasingly shallower (i.e., more “grey”) as  $\varepsilon$  grows and the second critical point is approached. This is due to the development of an increasingly strong *even* imaginary part of the solution. Furthermore, the stable background solution  $u_b(x)$  (cf. Eqs. (11) and top panel of Fig. 1) develops an *odd* imaginary part resembling a (progressively darker) grey soliton. Finally, at  $\varepsilon = \varepsilon_{\text{cr}}^{(2)}$ , the profiles of these modes become identical and disappear in a blue-sky bifurcation through their collision. In this saddle-center bifurcation, the dark soliton plays the role of the saddle, while the ground state of the system is the center. This observation leads to the conclusion that there is a “phase transition” where the system loses its  $\mathcal{PT}$ -symmetry, since the nonlinear problem eigenvalues become complex; this is in direct analogy with the so-called linear  $\mathcal{PT}$  “phase transition” as per the terminology of Ref. [1]. This will be discussed in more detail below.

However, we should highlight here that one more nontrivial question persists in the context of the single dark soliton. Past the critical point  $\varepsilon_{\text{cr}}^{(1)}$ , it is expected that the instability of the soliton at the center will provide us with “daughter states”

which are spontaneously symmetry broken dark solitons centered at a positive or at a negative value of  $x_0$ . For real chemical potentials/ propagation constants, such states can, nevertheless, not be identified. This appears to be inconsistent with the pitchfork nature of the bifurcation and constitutes a point to which we will return after we visit the dark soliton evolution to appreciate the dynamical implications of this instability.

## 4 Multiple Dark Soliton States and Nonlinear $\mathcal{PT}$ Phase Transitions

In this section, we will study higher excited states, in the form of multiple dark solitons. Such states are known to exist in the presence of  $V(x)$ , and have been studied extensively in the context of BECs [39, 41, 42]. Here, we will consider them in the presence of the imaginary part of the potential  $W(x)$ . Particularly, we will focus on the two- and three-dark-soliton states; qualitatively similar results can also be obtained for higher excited states.

### 4.1 Two-Dark-Soliton State

The density and phase of a two-dark-soliton-state are shown in the top panel of Fig. 3. Similarly to the ground state branch (see Fig. 1), we observe that a density dip is formed at the center, which becomes deeper as  $\epsilon$  is increased. Additionally, we observe that the two solitons are located away from the center, at some finite equilibrium distance  $\pm X$ . This equilibrium corresponds to the situation where the repulsive force between the solitons and the “expulsive” (with respect to the trap center) effect, for sufficiently large  $\epsilon$ , of the imaginary part of the potential  $W(x)$  analyzed in the last section is counter balanced by the confining nature of the real part of the potential  $V(x)$  [39, 41].

Below we will study analytically how the presence of the imaginary potential  $W(x)$  modifies the equilibrium distance  $X$  characterizing the stationary two-soliton-state, and also study small-amplitude oscillations of the solitons around their fixed points. To obtain an approximate equation of motion (analogous to Eq. (21)) for the two soliton centers, we assume that each of the two solitons feels the effective external potential of Eq. (19) and, at the same time, the solitons interact with each other. We assume that the pertinent interaction potential,  $V_{\text{int}}$ , for two (almost black) solitons, located at position  $x_1$  and  $x_2$ , has the form obtained from the exact two-soliton solution of the underlying unperturbed NLS system (see details in Ref. [41]), namely:

$$V_{\text{int}}(x_1, x_2) = \frac{\mu}{2 \sinh^2[\sqrt{\mu}(x_2 - x_1)]}. \quad (22)$$

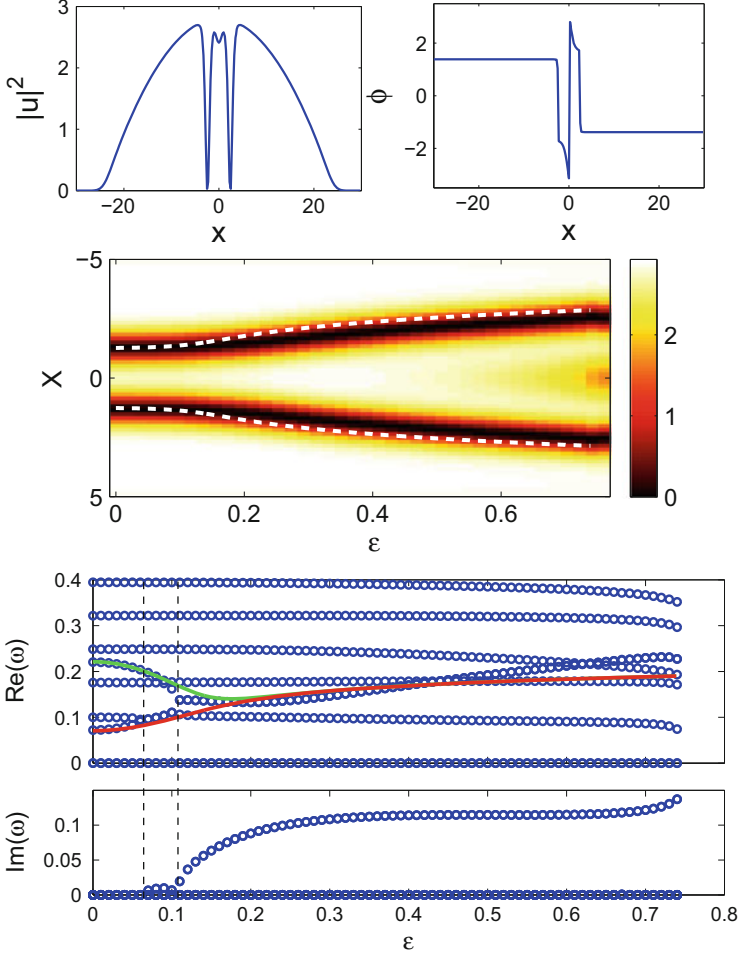


**Fig. 3** *Top panels:* the density (*left*) and phase (*right*) profiles of a stationary two-dark-soliton state. *Middle panel:* the dependence of the equilibrium configuration of the two-soliton solution as a function of  $\epsilon$ ; *dashed (white) lines* show the theoretical predictions for the position of the centers of the waves, cf. fixed points of Eqs. (24) and (25). *Bottom panels:* the linear spectrum of the two soliton branch, namely the real (*top*) and imaginary (*bottom*) parts of the eigenfrequencies as functions of  $\epsilon$ . *Solid red and green lines*, correspond to the analytical result of Eq. (30). The value of these modes at  $\epsilon = 0$ , corresponds to the first and second anomalous modes of the Hamiltonian case

The equation of motion for the two soliton centers ( $x_1$  and  $x_2$ ) can now be obtained from the Lagrangian:

$$L = \frac{1}{2}\dot{x}_1^2 + \frac{1}{2}\dot{x}_2^2 - V_{\text{eff}}(x_1) - V_{\text{eff}}(x_2) - 2V_{\text{int}}(x_1, x_2), \quad (23)$$

where the external effective potential  $V_{\text{eff}}$  is given in Eq. (19). Using the Euler-Lagrange equations, and assuming that the two solitons are far away from each other, i.e.,  $|x_2 - x_1| \gg 0$ , we approximate their mutual interaction term in Eq. (23) by its exponential asymptote and obtain the following equations of motion:

$$\ddot{x}_1 = -8\mu^{3/2}e^{-2\sqrt{\mu}(x_2-x_1)} - \tilde{\omega}^2 x_1 + \varepsilon^2 c_1 \text{sech}^4(c_2 x_1) \tanh(c_2 x_1), \quad (24)$$

$$\ddot{x}_2 = 8\mu^{3/2}e^{-2\sqrt{\mu}(x_2-x_1)} - \tilde{\omega}^2 x_2 + \varepsilon^2 c_1 \text{sech}^4(c_2 x_2) \tanh(c_2 x_2). \quad (25)$$

where  $\tilde{\omega} = \Omega/\sqrt{2}$  is the oscillation frequency of the single dark soliton in the absence of  $W(x)$  [39]. The fixed points  $X_2 = -X_1 = X$  of the above system can be found numerically, by setting the left-hand side equal to zero, and employing a fixed-point algorithm.

Next, we can study the stability of these equilibrium positions  $X_1$  and  $X_2$ , by considering small deviations,  $\eta_1$  and  $\eta_2$ , around them. By Taylor expanding the nonlinear terms, and keeping only linear terms in  $\eta_1$  and  $\eta_2$ , we derive the following set of linearized equations of motion:

$$\ddot{\eta}_1 = 16\mu^2 e^{-4\sqrt{\mu}X} (\eta_2 - \eta_1) - \tilde{\omega}^2 \eta_1 + \varepsilon^2 c_1 c_2 [5 \text{sech}^6(c_2 X) - 4 \text{sech}^4(c_2 X)] \eta_1, \quad (26)$$

$$\ddot{\eta}_2 = -16\mu^2 e^{-4\sqrt{\mu}X} (\eta_2 - \eta_1) - \tilde{\omega}^2 \eta_2 + \varepsilon^2 c_1 c_2 [5 \text{sech}^6(c_2 X) - 4 \text{sech}^4(c_2 X)] \eta_2. \quad (27)$$

Let us now consider the normal modes of the linearized system and seek solutions of the form  $\eta_i = \eta_i^0 e^{i\omega t}$ , where  $\omega$  is the common oscillation frequency of both dark solitons. Then, substituting this ansatz into Eqs. (26) and (27), we rewrite the equations of motion as a matrix eigenvalue equation, namely:

$$-\omega^2 \boldsymbol{\eta} = \begin{pmatrix} -\tilde{\omega}^2 + f(X) & 16\mu^2 e^{-4\sqrt{\mu}X} \\ 16\mu^2 e^{-4\sqrt{\mu}X} & -\tilde{\omega}^2 + f(X) \end{pmatrix} \boldsymbol{\eta}. \quad (28)$$

where  $\boldsymbol{\eta} = (\eta_1, \eta_2)^T$  and the function  $f(X)$  is given by:

$$f(X) = -16\mu^2 e^{-4\sqrt{\mu}X} + \varepsilon^2 c_1 c_2 [5 \text{sech}^6(c_2 X) - 4 \text{sech}^4(c_2 X)]. \quad (29)$$

To this end, it is possible to obtain from Eq. (28) the two characteristic frequencies

$$\omega_{1,2} = \sqrt{\tilde{\omega}^2 + f(X) \pm 16\mu^2 e^{-4\sqrt{\mu}X}}, \quad (30)$$

where  $\omega_1$  ( $\omega_2$ ) correspond to the in-phase (out-of-phase) oscillations of the two solitons [39, 41].

The validity of the above analytical result can now be compared with the corresponding numerical result obtained by the numerical existence theory and

the BdG analysis. The latter provides the equilibrium configuration, as well as the real/imaginary parts of the eigenfrequencies as functions of the imaginary potential strength  $\varepsilon$ , as shown in the middle and bottom panels of Fig. 3, respectively. In the middle panel, we can observe a very good agreement between the positions of the theoretically predicted solitary wave centers (cf. the fixed points of Eqs. (24) and (25)) and their numerically exact counterparts.

For the linearization analysis of the bottom panels, we observe the following. In the Hamiltonian case, there exist two anomalous modes (and more generally,  $n$  anomalous modes for a  $n$ -soliton state—see, e.g., Ref. [39]). The first, which is the lowest nonzero mode in the spectrum, corresponds to the in-phase oscillation frequency of the two dark solitons, while the second being the fourth finite eigenfrequency for our parameters, corresponds to out-of-phase oscillations. The two-soliton branch is initially stable up to a critical point (indicated by the left vertical line), where the first finite mode collides with the dipole (alias Kohn) mode [39]; this mode is located, for  $\varepsilon = 0$ , at  $\text{Re}(\omega) = \Omega = 0.1$ . This collision results in the emergence of an instability, which is identified by the appearance of an imaginary part of the eigenfrequency (see the bottom panel of Fig. 3). As  $\varepsilon$  is increased, this mode is eventually *detached* from the dipole mode and this instability band ceases to exist for a very narrow parametric interval. However, the quadrupole mode (located, for  $\varepsilon = 0$ , at  $\text{Re}(\omega) \approx \sqrt{3}\Omega = 0.17$ ), which has been scattered at about  $\varepsilon = 0.08$ , by the branch just above, now collides with the detached mode (right vertical line). Upon the latter collision, a new (and persistent hereafter) second instability emerges (see the bottom panel of Fig. 3). This way, another quartet of complex eigenfrequencies is created, indicating that the two-soliton state becomes unstable with a growth rate that continues to increase as the gain/loss parameter  $\varepsilon$  increases.

The analytical result for the two eigenfrequencies  $\omega_{1,2}$  (cf. Eq. (30) and solid red and green lines in Fig. 3) essentially coincides with the two branches initialized at the two anomalous modes of the Hamiltonian case, for sufficiently small  $\varepsilon$ ; however, for larger  $\varepsilon$ , the analytical result is somewhat less accurate. The observed discrepancy is, at least in part, due to the fact that our approximate result is based on a particular ansatz of well-separated (thus weakly-interacting), almost black solitons. However, observing the density profile of the two soliton state (top panel of Fig. 3), one can see that the small density dip in the center (which is not included in our ansatz) is certainly affecting the interaction between the two solitons; importantly, this dip becomes larger as  $\varepsilon$  is increased. Thus, for relatively large values of  $\varepsilon$ , our perturbative approach may be expected to be of lesser value.

Additionally we note that, as in the case of the single-soliton-state, for values  $\varepsilon > 0.72$  no stationary two-soliton-state could be identified. This is again a by-product of the nonlinear analogue of the  $\mathcal{PT}$ -phase transition. More specifically, the two-soliton branch collides with the three-soliton one and they pairwise annihilate, as is occurring to higher (linear) eigenvalue pairs in the linear  $\mathcal{PT}$ -phase transition of Ref. [1]. We illustrate the generality of this effect (and the relevant cascade of nonlinear eigenvalue collisions) in more detail below.

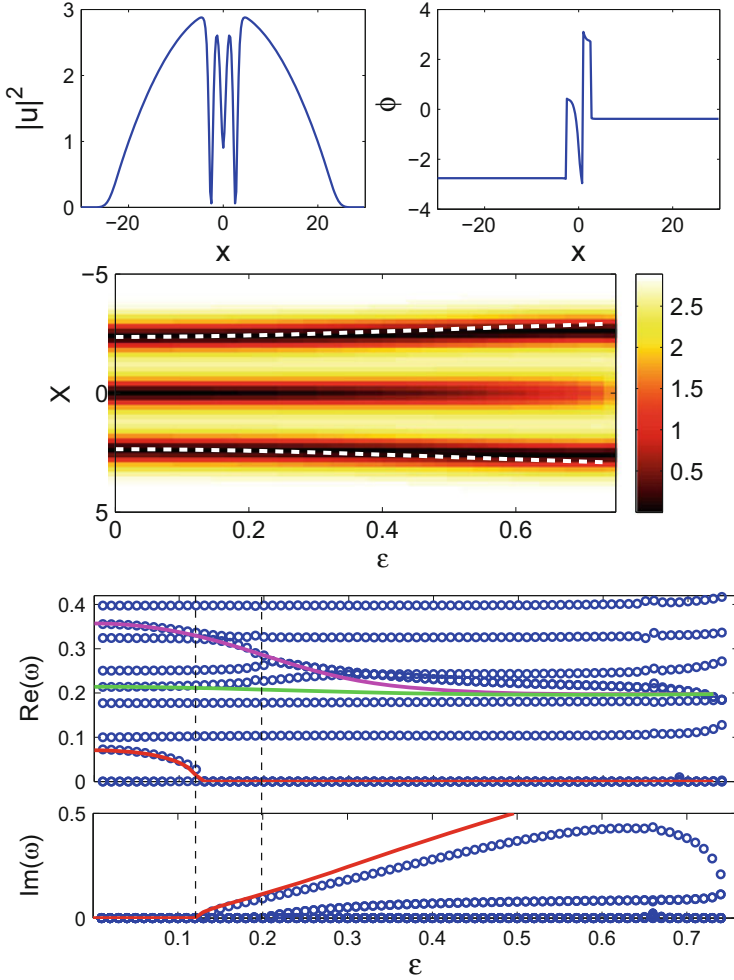


**Fig. 4** Same as Fig. 3, but for the three soliton state. In the *bottom panels*, *solid red, green and magenta lines*, correspond to the analytical result of Eqs. (31) and (32). The value of these modes at  $\epsilon = 0$  correspond to the first, second and third anomalous modes of the Hamiltonian case

## 4.2 Three-Dark-Soliton State

We now proceed with the investigation of the three-soliton branch; examples of the density and phase of such a state are shown in the top panel of Fig. 4. This state shows similar behavior with the single soliton state, in the sense that the soliton located at the center becomes shallower as  $\epsilon$  is increased.

The statics and dynamics around equilibria of the three-dark-soliton state can be analyzed by the methodology adopted in the case of the two-dark-soliton state.

Particularly, we will determine the equilibrium positions of the three solitons and study their small-amplitude oscillations around their fixed points. First we note that, from symmetry arguments, we expect that the fixed points are  $X_2 = 0$  (for the central soliton), and  $X_3 = -X_1 = X$  (for each of the two outer solitons). For this configuration, we can again calculate the fixed points for the outer solitons numerically and compare them to the particle theory analytical predictions, as illustrated in the middle panel of Fig. 4, obtaining good agreement for small values of  $\varepsilon$ .

Subsequently, we derive the linearized equations around the fixed points, and finally obtain the three relevant eigenfrequencies of the system. This way, we find that the frequencies of the normal modes of the system are:

$$\omega_1 = \sqrt{f_1(X)} \quad (31)$$

$$\omega_{2,3} = \left\{ \frac{1}{2} f_1(X) \pm f_2(X) \left[ (f_1(X) - f_2(X))^2 + 8f_3(X)^2 \right]^{1/2} \right\}^{1/2}, \quad (32)$$

where functions  $f_i(X)$  ( $i = 1, 2, 3$ ) are given by:

$$f_1(X) = \tilde{\omega}^2 - 16\mu^2 e^{-2\sqrt{\mu}X} + \varepsilon^2 c_1 c_2 [5 \operatorname{sech}^6(c_2 X) - 4 \operatorname{sech}^4(c_2 X)], \quad (33)$$

$$f_2(X) = \tilde{\omega}^2 - 32\mu^2 e^{-2\sqrt{\mu}X} + \varepsilon^2 c_1 c_2, \quad (34)$$

$$f_3(X) = 16\mu^2 e^{-2\sqrt{\mu}X}. \quad (35)$$

The above characteristic frequencies will again be compared to the eigenfrequencies obtained numerically by means of the BdG analysis. For this purpose, in the bottom panels of Fig. 4, we show the BdG linear spectrum of the three-dark-soliton branch.

As observed in the figure, the three-dark-soliton state is initially stable (for sufficiently small  $\varepsilon$ ), but it becomes unstable after a collision of the lowest mode (dashed (red) line) with the spectral plane origin, giving rise to the emergence of an imaginary pair of eigenvalues. This is directly reminiscent of the corresponding instability of the single dark soliton state and the mechanism of the instability is expected to persist for *any* configuration with an odd number of dark solitons in this system (we have also checked that it arises in the case of a five-soliton state). For larger values of  $\varepsilon$ , another collision between the fifth and sixth mode, results in the emergence of an imaginary eigenfrequency pair (right vertical dashed line), and thus the three soliton state remains unstable.

At the same time, and as in the single-soliton case, the imaginary eigenfrequency corresponding to the first nonzero mode, eventually returns to the origin and collides with it, at  $\varepsilon = 0.72$ . This is the critical point of the collision of the two-soliton and the three-soliton branch and of their pairwise annihilation. As the relevant critical value of  $\varepsilon$  is approached, the center grey soliton of the three-soliton state becomes grayer and eventually becomes identical to the central density dip of the two-soliton state with which it collides. The above characteristic frequencies will again be compared to the eigenfrequencies obtained numerically by means of the

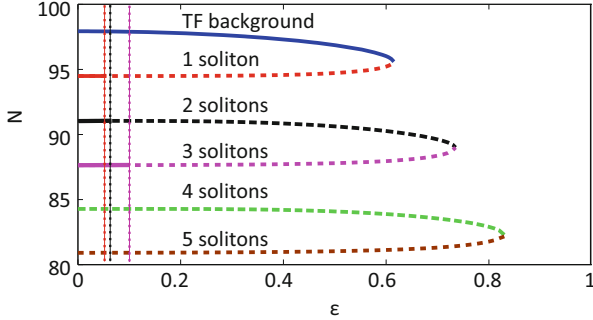


**Fig. 5** The power  $N$  as a function of  $\varepsilon$ , for the six lowest states. *Solid lines* correspond to linearly stable states and *dashed lines* to unstable states, with  $\text{Im}(\omega) \neq 0$ . The *vertical lines* denote the critical values of  $\varepsilon$  found for the single-, two- and three-dark-soliton states. This bifurcation diagram illustrates the nonlinear  $\mathcal{PT}$ -phase transition points, at which stationary states disappear in pairs through blue-sky bifurcations

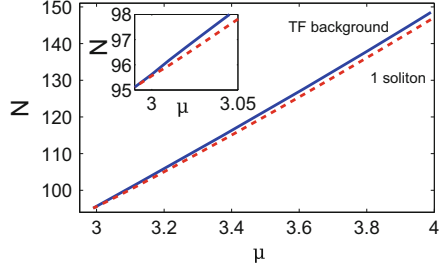
BdG analysis. For this purpose, in the bottom panels of Fig. 4, we show the BdG linear spectrum of the three-dark-soliton branch.

The analytical results for the three eigenfrequencies (cf. Eqs.(31) and (32) and solid red, green and magenta lines in Fig. 4) are in a good agreement with the respective modes obtained numerically via the BdG analysis, as long as  $\varepsilon$  is sufficiently small. In particular, the critical value of  $\varepsilon$  where the first finite mode collides with the origin (thus giving rise to the instability) is very well predicted; furthermore, the analytically found “trajectory” of the other two branches follow, in a fairly good accuracy, the respective numerical result, even for moderate and large values of  $\varepsilon$ , with an expected progressive discrepancy as  $\varepsilon$  becomes large (when the problem is outside the realm of a perturbative treatment).

### 4.3 Nonlinear $\mathcal{PT}$ Phase Transitions

In order to further elaborate on the emergence of the nonlinear  $\mathcal{PT}$ -phase transition, in Fig. 5 we plot the power  $N$  as function of the parameter  $\varepsilon$ , for the lowest six (ground state and the first five excited) states of the system. The top solid (blue) branch depicts the stable ground state (i.e., the TF background  $u_b$ —cf. Eqs. (9)–(11)), which ultimately collides with the single-dark-soliton branch (dashed (red) line), i.e., the first excited state at  $\varepsilon \approx 0.62$  (for  $\mu = 3$ ). Furthermore, the next pair of branches, corresponding to the two- and three-dark-soliton states (depicted by the dashed black and magenta lines, respectively), also collide at  $\varepsilon \approx 0.72$ . This picture of colliding and annihilating pairs of excited states remains the same even for higher excited states—cf. the lowest dashed (green and brown) curves in Fig. 5, showing the annihilation of the five- and six-dark-soliton states as well.

**Fig. 6** The power  $N$  as a function of  $\mu$ , for the TF branch (solid (blue) line) and the single-soliton branch (dashed (red) line, indicating instability); the two branches collide approximately at  $\mu = 3$ . The gain/loss parameter is  $\varepsilon \approx 0.613$  and the trap strength is  $\Omega = 0.1$



An important general remark, regarding the structure of the bifurcations shown in Fig. 5, is that higher excited states sustain these collisions, saddle-center bifurcations and corresponding blue-sky annihilations for progressively larger values of  $\varepsilon$ . This feature motivates us to refer to this process as the *nonlinear analogue* of the “traditional”  $\mathcal{PT}$  transition, in direct correspondence with the pairwise collisions in Ref. [1] (see, e.g., Fig. 1 of that reference) for the linear setting. Although the two figures are similar, there are some interesting differences. One such is that in the linear picture the lowest eigenvalues collide the last, while in the 1D nonlinear case the lowest eigenstates disappear first.<sup>1</sup> This feature has important consequences for the supercritical evolution of the system which we will revisit in the dark soliton dynamics section below.

To conclude this section we also add the following comments and compare our results with those reported in Ref. [27]. In the latter work, a bifurcation diagram  $N(\mu)$  was obtained, where pairs of branches starting from the *linear* limit collided and disappeared in the nonlinear regime with the defocusing nonlinearity. Such a form of the bifurcation diagram was due to the assumed form of the  $\mathcal{PT}$ -symmetric potential, which allowed for the existence of linear eigenstates with real eigenvalues for all values of the gain/loss coefficient. However, in our case, progressively more linear eigenstates acquire complex—rather than real—eigenvalues past corresponding critical (maximum) values of the gain/loss coefficient  $\varepsilon$ . As a result, a  $N(\mu)$  bifurcation diagram in our case would typically have a considerably different form than the one of Ref. [27]: starting from the highly nonlinear Thomas-Fermi regime (where  $\mu/\Omega \gg 1$  and the length scale of the solitary waves is much shorter than that of the condensate) and decreasing  $\mu$ , pairs of branches would collide at a critical value of  $\mu$  and disappear via a saddle-center bifurcation. This behavior is shown in Fig. 6 for a value of  $\varepsilon \approx 0.613$  where the first two branches, i.e. the TF branch and the one-soliton branch, coming from the far nonlinear limit with decreasing  $\mu$ , collide at  $\mu = 3$ . For smaller  $\mu$ , only states with complex  $\mu$  exist. For this value of  $\varepsilon$ , we have numerically obtained the first two linear eigenvalues:  $\lambda_{1l} \approx 0.149 + 0.093i$

<sup>1</sup>Another important difference that we do not touch upon here is that in the model of Ref. [1], the ground state does not collide with some other linear mode of the system, contrary to what is the case herein.

and  $\lambda_{2l} \approx 0.283 + 0.034i$ , which are complex, and thus one does not expect to find nonlinear states bifurcating from these two linear states.

#### 4.4 The “Free Space” Case

In our previous considerations, we have studied the case where the real part of the external potential was parabolic. Nevertheless, and as a complementary setting, it is also interesting to consider the “free space” case, where the real trapping potential is absent, i.e.,  $V(x) = 0$ . Such a situation may occur, e.g., in the context of optics where—instead of a graded index medium—one may consider a medium with a constant linear refractive index, i.e.,  $V(x) = V_0 = \text{const.}$ ; in this case, the pertinent term  $V_0 u$  that would appear in Eq. (1) can straightforwardly be removed by a trivial gauge transformation.

An interesting feature characterizing the free space case is that stationary multiple dark soliton states can no longer exist: in this case, the repulsion between dark solitons cannot be counter balanced by any restoring force as the  $V(x)$  producing the latter is absent. As a result, the most fundamental states pertinent to this setting are the ground state and the single-dark-soliton state. An approximate solution for the free-space ground state  $u_0$ , can be found employing Eq. (11) and setting  $V(x) = 0$ , namely:

$$u_0 = \mu - \frac{1}{\sqrt{\mu}} \mathcal{W}^2(x) \exp\left(2i \int \mathcal{W}(x) dx\right). \quad (36)$$

Using the above result, and following the analysis of the previous sections, we find that the evolution of the dark soliton center is described by (cf. Eq. (21)):

$$\frac{d^2 x_0}{dt^2} = \frac{6}{5} \varepsilon^2 x_0. \quad (37)$$

The above equation dictates that a quasi-stationary (almost black) dark soliton is always unstable for *any finite*  $\varepsilon$ , since it experiences an effective expulsive force, which tends to displace it from the origin and set it into motion with an increasing (magnitude of) acceleration, at least for small values of  $x_0$ . This is in contrast to the case of a parabolic  $V(x)$ , where the respective force exerted on the soliton and the effective expulsive force induced by the imaginary potential  $\mathcal{W}(x)$  could balance each other. Thus, the presence of the real parabolic trap (or, more generally, of a confining potential) is crucial for the existence of stable stationary soliton solutions.

The top panel of Fig. 7 shows the relevant eigenfrequency for the linear stability spectrum of the dark soliton, with respect to the parameter  $\varepsilon$ . As predicted by Eq. (37), as soon as  $\varepsilon$  becomes non-vanishing, the dark soliton becomes unstable. Its spectrum shows a pair of imaginary eigenfrequencies emerging from the spectral plane origin in good agreement (for small/intermediate values of  $\varepsilon$ ) with the

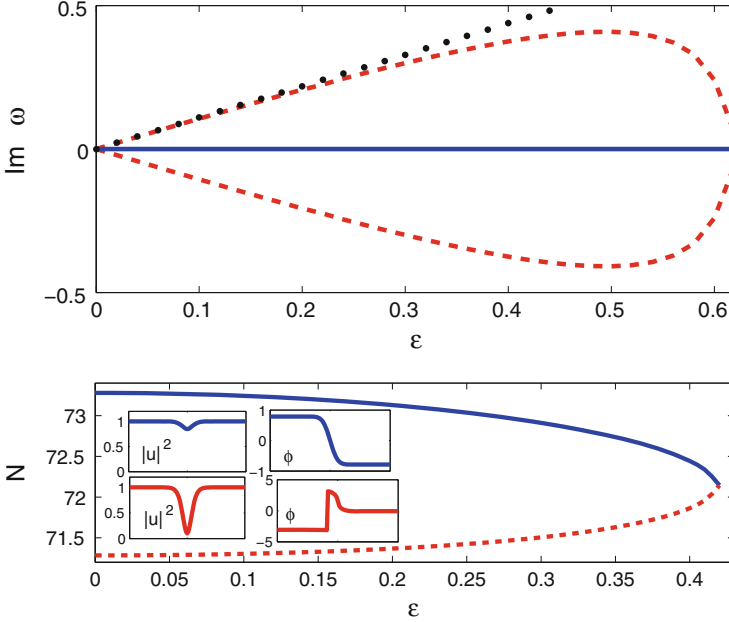


**Fig. 7** *Top panel:* pertinent eigenfrequency of the linear spectrum for the free-space dark soliton with respect to  $\epsilon$ . *Dashed (red) line* depicts the imaginary eigenfrequency pair arising due to the presence of  $W(x)$  and the *dotted line* represents the corresponding theoretical prediction. *Bottom panel:* the  $\mathcal{PT}$ -phase transition diagram in the  $(N, \epsilon)$  plane. *Solid (blue) line* shows the background branch, while *dashed (red) line* the single-dark-soliton state. The *upper* and *lower insets* show characteristic densities and phases for the ground state and the dark soliton, respectively. In this case,  $\mu = 1$

corresponding theoretical prediction. Similarly to the case with the real parabolic potential (see Fig. 2), this pair of eigenfrequencies eventually returns to—and collides with—the spectral plane origin, signaling the termination of the branch and the  $\mathcal{PT}$ -transition. In the bottom panel of Fig. 7, the bifurcation diagram for the ground state and the single-dark-soliton in the free-space case is plotted; we observe a behavior similar to the one found in the case with the parabolic  $V(x)$ , but with the major difference that beyond the critical point ( $\epsilon \approx 0.43$  in this case) *no stationary states* exist, as the only ones such have collided and disappeared in the saddle-center bifurcation discussed above.

## 5 Dark Soliton Dynamics

We continue by considering the dynamics of the nonlinear excited states, by numerically integrating Eq. (1) in various different regimes in  $\epsilon$ . To be more specific, our aim is to illustrate the dynamics of the dark soliton upon its destabilization after

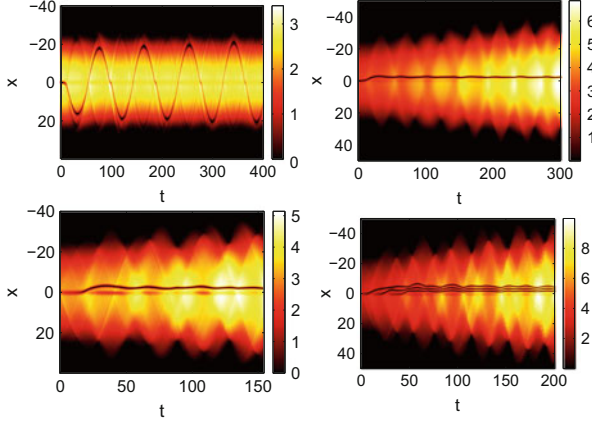


**Fig. 8** Bifurcation-induced dynamics. *Top panels*: two potential manifestations of the SSB destabilization scenarios for a single unstable dark soliton past  $\varepsilon = \varepsilon_{\text{cr}}^{(1)} \approx 0.066$ . *Bottom panels*: soliton “sprinklers” spontaneously leading to a single dark soliton (*left*) and the formation of three dark solitons (*right*), using as an initial condition the ground state for  $\varepsilon > \varepsilon_{\text{cr}}^{(2)} \approx 0.62$ . The parameters are  $\mu = 3$  and  $\Omega = 0.1$  and  $\varepsilon = 0.4$  (*top row*),  $\varepsilon = 0.63$  (*bottom left*), and  $\varepsilon = 0.66$  (*bottom right*)

the SSB bifurcation at  $\varepsilon_{\text{cr}}^{(1)}$ , and also beyond the nonlinear  $\mathcal{PT}$ -phase transition. Generally, to study the dynamics of unstable solitons, we prepare a stationary dark soliton solution in the unstable regime (dashed parts of the soliton branches in Fig. 5), we add a small random perturbation, and then allow the resulting configuration to evolve in time. We have found that the dynamics of the system strongly depends on whether the soliton will be displaced—as a result of the instability—towards  $x > 0$  (the “gain side” of  $W(x)$ ) or  $x < 0$  (the “lossy side” of  $W(x)$ ).

First, we consider a case where a dark soliton is spontaneously ejected to the gain side of the imaginary potential; a pertinent example is shown in the top left panel of Fig. 8. It is observed that, in this case, the solitary wave starts to perform oscillations of large amplitude, a behavior which is generic for all solitons that are initially located at  $x > 0$ . On the other hand, if the soliton is initially kicked towards the “lossy” side of  $W(x)$ , upon an initial displacement of a finite  $\varepsilon$ -dependent size, it stops moving and remains quiescent, while the background on which it “lives” begins to grow in amplitude and width. A relevant example is illustrated in the top right panel of Fig. 8. We once again highlight the apparent incompatibility of the above scenarios with the expectation of a double well effective potential for the soliton and the SSB bifurcation of the soliton at  $x_0 = 0$ . This paves the way for the examination of the ghost states in the next section. For completeness, we also show the evolution of the power  $N(t) = \int |u(x, t)|^2 dx$  in the top panels of Fig. 9, for both the above scenarios. In the left panel, which corresponds to the oscillating dark soliton, the power (after a short time interval during which it decreases) oscillates

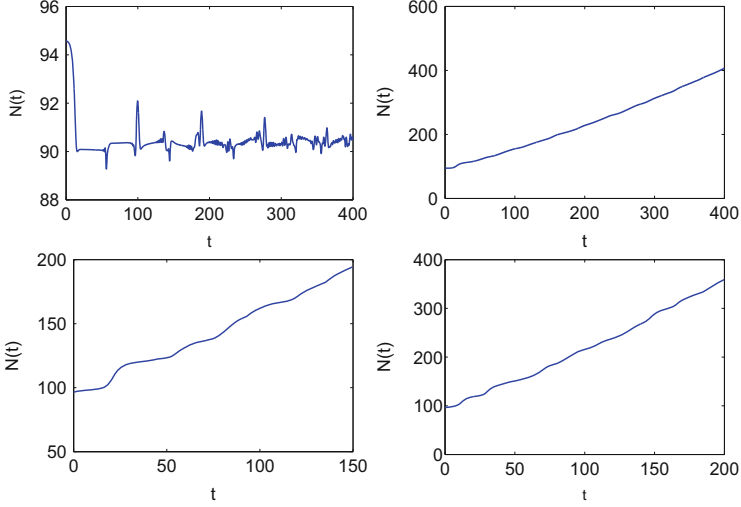


**Fig. 9** Evolution of the power  $N(t)$ ; each panel corresponds to the respective panels of Fig. 8. The *top left panel*, pertaining to the case of an oscillating dark soliton, exhibits oscillatory behavior. In all other cases the power is monotonically increasing

around a fixed value of  $N \approx 90$ . On the other hand, in the case of an unstable soliton localizing on the lossy side of  $W(x)$ , the power is monotonically increasing with time, as depicted in the top right panel of Fig. 9. The above two cases are the prototypical possibilities (independently of  $\varepsilon$ ) for the fate of the dark soliton upon its destabilization, when the dark soliton state still exists.

We now turn to the examination of what happens beyond  $\varepsilon = \varepsilon_{\text{cr}}^{(2)}$  (where the TF background and the single soliton are no longer stationary solutions of Eq. (1)). There, we use, e.g., an initial condition in the form of a TF background  $u(x, 0) = \sqrt{\mu - V(x)}$ , pertinent to the conservative system [30] as a means of exploring how the system responds when its fundamental states are no longer present. We have found that a dark soliton train is spontaneously formed, with an increasingly larger number of solitons as larger values of  $\varepsilon$  are employed. The bottom two rows of panels of Fig. 8 depict two examples of this phenomenon. This constitutes a form of what can be dubbed a “soliton sprinkler”. This can, at least in part, also be intuitively connected to the observation of Fig. 2 that higher excited multi-soliton states persist for larger  $\varepsilon$  than lower ones. Nevertheless, it should also be highlighted that the observations typically suggest that the solitons are nucleated and stay in the vicinity of the global minimum of  $W(x)$ , and more generally tend to become stationary residing on the “lossy” side of the imaginary potential, similarly to the dynamical state observed above and accompanied by the same kind of background growth. The time evolution of the power for these multi-soliton states is shown in the bottom panels of Fig. 9; in both cases, the power increases monotonously with time, in line

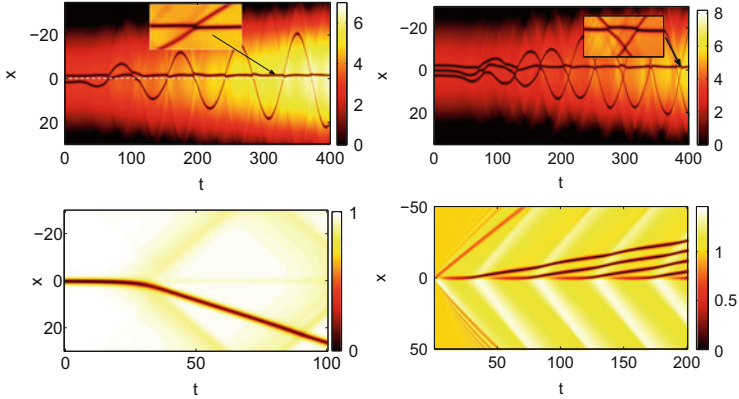


**Fig. 10** Bifurcation-induced dynamics. *Top panels*: Manifestation of the dynamical instability of the two soliton state (oscillatory instability of the *top left panel*) and of the three soliton state (exponential and oscillatory instability of the *top right panel*). Both end up with one solitary wave sitting on the lossy side and the rest impinging on it through collisions between turning points within a continuously growing background. The *bottom panel* shows the case without  $V(x)$  where the single soliton manifests its instability by being set into motion (*bottom left panel*), while a uniform initial condition past the  $\varepsilon_{\text{cr}}^{(2)}$  starts emitting dark solitons in the form of a sprinkler. The parameters are  $\mu = 3$  and  $\Omega = 0.1$  and  $\varepsilon = 0.4$  (*top left*),  $\varepsilon = 0.4$  (*top right*), while  $\mu = 1$  and  $\varepsilon = 0.1$  (*bottom left*), and  $\varepsilon = 0.45$  (*bottom right*)

with the localization of such solitary waves on the lossy side of the potential (cf. top right panel of Figs. 8 and 9).

As an additional aspect of the investigation of the dynamics of higher-excited (multi-soliton) states, and how their instabilities manifest themselves when they are subject to small perturbations, we consider the runs of the top panel of Fig. 10. In the left panel, the dynamics of a two-soliton state is shown. At  $t = 0$  the two solitons are in equilibrium, but the soliton on the gain side starts to execute oscillations within the trap, as was the case before in Fig. 8 for the soliton displaced towards the gain side (top left panel of the figure). Thus, inevitably, this soliton, upon hitting a turning point in its oscillation, returns and collides with the other one. The result of the multiple collisions that ensue is that one of the solitons continues to execute oscillations of increasing amplitude while the other one remains effectively stationary on the lossy side. While the above sequence of oscillations and collisions is continuously repeated, at the same time, the background grows both in amplitude and width. It is interesting to note that the two solitons behave in a way that resembles a combination of the two different scenarios observed in the single soliton case, with the relevant dynamics resembling a “superposition” of the ones shown in the top two panels of Fig. 8. Yet there is one non-trivial difference. While the amplitude of oscillation in the top left panel of Fig. 8 remains roughly unaltered, the one of the top left panel of Fig. 10 keeps increasing due to the continuously

expanding background (which, in turn, shifts the turning point of the corresponding oscillation).

A similar behavior is also found in the case of three solitons, as shown in the top right panel of Fig. 10. Two of the three solitons are now oscillating inside the harmonic potential while the third one is trapped in the lossy side of the potential. As the solitons pass through the origin, they perform their respective oscillations and undergo collisions, in a procedure which is continuously repeated; at the same time, once again, the background is growing and this, in turn, leads to a growth of the turning points of the nearly alternating oscillations of the two non-stationary solitons.

We now compare the above results to the ones corresponding to the free-space case, i.e., when the trapping potential  $V(x)$  is absent. Recall that in this case only two stationary solutions exist (the ground state and the single soliton) and the soliton is always unstable. Since the background wave is now of constant density, when the soliton is perturbed, it will start to move away from the origin and will accelerate according to Eq. (37) up to the point where it is practically no longer under the influence of the (exponentially localized) imaginary part of the potential. Thereafter, it will acquire a nearly constant velocity and will keep moving in that direction, as shown in the bottom left panel of Fig. 10 (the absence of the real part of the potential leads to a lack of a turning point in this case).

Finally, we consider the parameter regime  $\varepsilon > \varepsilon_{\text{cr}}$ , i.e., after the occurrence of the  $\mathcal{PT}$ -phase transition where no stationary solutions exist. We numerically integrate Eq. (1), with an initial condition of the form of a plane wave  $|u(x, 0)| = \sqrt{\mu}$ , and the result is shown in the right bottom panel of Fig. 10. The initial plane wave begins to emit dark solitons, which are all starting to propagate along the “lossy” direction. Contrary to the confined case where the trapping potential was keeping the solitons near the origin, the solitons are continuously created and are now free to propagate along the  $x$  axis. Hence, once the “sprinkling” process begins, it continues indefinitely.

## 6 Ghost States and Their Dynamical Role

It is now relevant to try to address some of the remaining questions, concerning the nature of the daughter states within the pitchfork bifurcation (of Fig. 2 and by extension e.g. in Fig. 4) and the unexpected asymmetric behavior of the dynamical evolution of unstable dark solitary waves in Fig. 8. A related issue concerns the feature that solitary waves become stationary on the lossy side of the potential (while the corresponding background starts growing); see Fig. 8 and by extension also Fig. 10.

A first way to try to address this problem is to consider the possibility (as suggested by the direct numerical simulations) of a state involving a stationary dark solitary wave off of  $x_0 = 0$  (and, in particular, for  $x_0 < 0$ ). Then the steady state problem would read:

$$\mu u = \mathcal{L}u + iWu + |u|^2u, \quad (38)$$

where  $\mathcal{L}$  is used to denote the linear, Hermitian part of the right hand side operator. The corresponding conjugate equation then reads:

$$\mu^* u^* = \mathcal{L}u^* - iWu^* + |u|^2u^*. \quad (39)$$

Now, by multiplying Eq. (38) by  $u^*$ , and Eq. (39) by  $u$ , integrating and subtracting the second equation from the first, we obtain the self-consistency condition for the imaginary part of the chemical potential:

$$\text{Im}(\mu) = \frac{1}{N} \int W(x)|u|^2 dx. \quad (40)$$

Interestingly, the right hand side is directly related to the one arising in Eq. (7) and, thus, also controls the time dependence of the atom number/optical power (or mathematically the  $L^2$  norm).

The key realization that emerges from Eq. (40) is that since  $|u|^2$  is an even function for solitary structures centered at  $x_0 = 0$  (and  $W(x)$  is anti-symmetric), the only way for our states to be centered at  $x_0 \neq 0$  is if  $\mu_I \equiv \text{Im}(\mu) \neq 0$ . However, this is an atypical feature for states arising in the context of the nonlinear Schrödinger (NLS) equation. More specifically, a fundamental underlying assumption behind the identification of stationary states, critically employing the U(1) invariance of the model, is the use of the product ansatz for stationary states of the form  $u(x, t) = e^{-i\mu t} f(x)$ . Now, we find ourselves at a junction where solutions may exist with a complex  $\mu$ . This, more specifically, implies that they will be indeed exact solutions of the *stationary* NLS problem, yet their incompatibility with the above ansatz *precludes* them from being exact solutions of the original dynamical problem of Eq. (1).

The natural next questions then involve whether these states can, in fact, be identified as such (exact solutions of the steady state problem) and, perhaps more importantly, what is their role in the observed dynamics. The first of these questions is answered in Fig. 11, where we have performed a continuation of these states as a function of  $\varepsilon$ , starting from the Hamiltonian limit in the absence of gain/loss. The top left panel of the figure presents the center of the solution as a function of the parameter, while the top right one evaluates the imaginary part of the chemical potential, by self-consistently enforcing the condition (40). It is key to mention here that for the solutions with negative  $x_0$ , it is straightforward to see that they correspond to a setting with  $\mu_I > 0$  (from Eq. (40)). On the other hand, the term  $e^{-i\mu t}$  will then involve a part associated with  $e^{-i(i\mu_I)t}$  and hence this state will be associated with growth over time. On the other hand, the state with  $\mu_I < 0$  will be connected to decay over time and does not appear to be relevant for physical observations. It is for that reason that one of the two states (the robust one) is denoted with a bold solid line in the top panels of Fig. 11, while the other one is denoted by

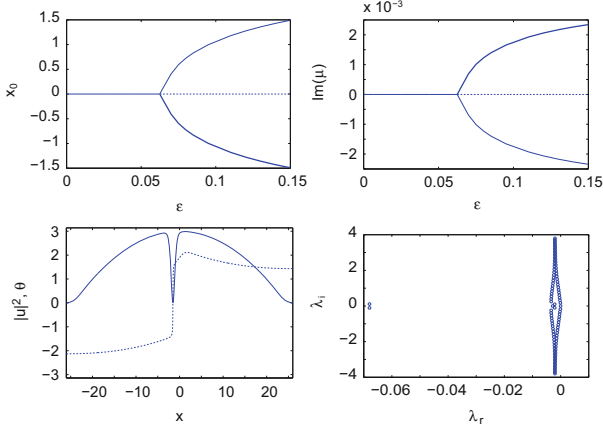


**Fig. 11** Properties of the ghost states. The *top left panel* illustrates their (off-center) location with the *bold line* illustrating the dynamically robust one. The *center line* corresponds to the dark soliton at  $x_0 = 0$  and the *solid to dashed* transition corresponds to the SSB bifurcation. Another diagram illustrating the pitchfork character of the transition is given in the *top right panel* through the imaginary part of the chemical potential  $\mu_I$  as a function of the gain/loss parameter. Again, the persisting state is given in *bold*. A typical example of the squared density and phase (*solid and dashed*, respectively) of a ghost state for  $\varepsilon = 0.15$  is given in the *bottom left panel*. Finally, a suggestive linear stability analysis (as if this were a true steady state of the system) is performed on the *bottom right* suggesting also the dynamical robustness of the relevant state due to the absence of eigenvalues with a positive real part (i.e., of ones corresponding to growth)

a thin line (and unstable states centered at  $x_0 = 0$  in the diagram are denoted by a dashed line).

First of all, this observation restores the canonical (and expected) pitchfork nature of the observed bifurcation (see top panels of Fig. 11 and the daughter state of the bottom left panel). But, at the same time it reconciles that nature with the absence of any “regular” daughter states. A stability analysis of these states is not particularly meaningful per se (as these are not stationary states of the original problem), yet it is natural to expect that it will be suggestive regarding the evolution of perturbations in the vicinity of such states. This, as shown in the bottom right panel for the displaced state of the bottom left one in Fig. 11, illustrates the effective stability of the resulting ghost state.

We now turn to the dynamical implications of the existence of such ghost modes. The asymmetry between the growth of the mode with the dark soliton at  $x_0 < 0$  and the decay of the one with  $x_0 > 0$  justifies the observed asymmetry of the dynamical evolution of the perturbations in Fig. 8. To illustrate the relevance of the ghost states in the case where the random perturbation manifests the instability of the  $x_0 = 0$  soliton by kicking it to the left, we performed some relevant numerical experiments in Fig. 12, for  $\varepsilon = 0.15$ . Specifically, by initiating the soliton at  $x_0 = 0$ , we confirm that it goes and sits precisely at the location (for that particular  $\varepsilon$ ) where the ghost state has the soliton centered (cf. with the out of scale profile of the shifted soliton

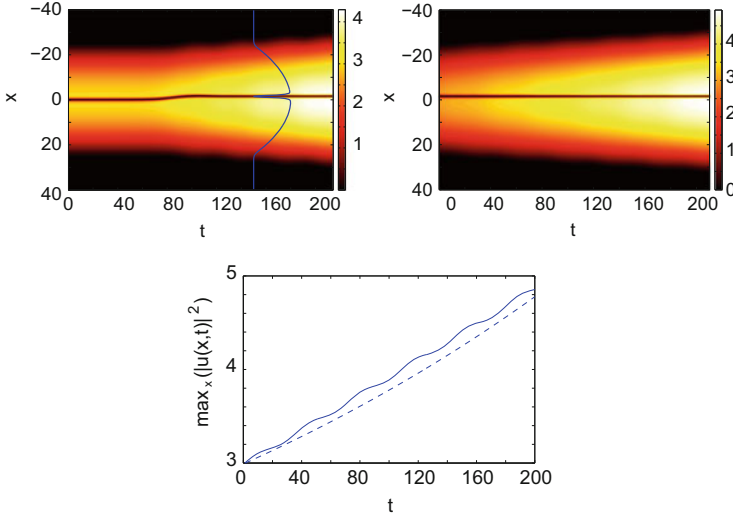


**Fig. 12** The *top left panel* shows the space-time evolution of the contour plot of the unstable dark soliton at  $x_0 = 0$  for  $\varepsilon = 0.15$ . For comparison (and out of scale), we plot (using a *solid (blue) line*) the exact obtained ghost state for the same gain/loss parameter. Clearly the dynamics gets attracted to this state, as is also corroborated by its evolution as initial condition in the *top right panel* (the dark soliton stays put, but the background width and amplitude grows in a way directly analogous to the case on the *left*). Finally, the comparison of the amplitude background growth  $A(t)$  (*solid line*) with the law implied by the growth rate of the ghost state  $A(t) = A(0) \exp(\mu_I t)$  (*dashed*) is shown on the *bottom panel*, suggesting good agreement between the two

within the graph). On the other hand, for a clear comparison, in the *top right panel* of Fig. 12, we have evolved the dynamical equations with exactly that proper ghost state for the particular  $\varepsilon$  as initial condition (wherein the soliton is located at  $-1.5$  for  $\varepsilon = 0.15$ ; see the right panel of the figure). The dynamics clearly illustrates that the soliton stays immobile (as expected by the nature of the ghost state), while the background increases in amplitude and also the width of the solution increases. These latter growth features are strongly reminiscent of the evolution of the left panel of the figure past the point of destabilization and convergence to a solitary wave centered at  $x_0 = -1.5$ . To further cement this proximity, we have computed the growth of the background amplitude i.e., the maximum absolute value of the field  $A(t)$  and have directly compared it to the simplistic law (implied by the ghost state growth rate  $\mu_I$ )  $A(t) = A(0) \exp(\mu_I t)$ , yielding the kind of agreement shown in the bottom panel of the figure. The natural conclusion is that while the ghost states are not genuine (steady) attractors of the original dynamics, nevertheless the evolution of the system closely shadows the relevant states and utilizes their asymmetry.

As for the case where the dark soliton moves to  $x_0 > 0$  due to the perturbation, then the ghost state is simply untenable as a dynamical state (due to its decay in time), hence the dark soliton proceeds to escape from the region of influence of the

gain and moves towards a turning point. This motion imparts sufficient momentum to the solitary wave that it can subsequently execute oscillations around  $x_0 = 0$ , as shown in Fig. 8 (top right). Moreover, dynamical features such as the generation of multi-solitons sitting on the lossy side can be explained upon the consideration of ghost states associated with multi-soliton states (see e.g. the 3-soliton state of the bottom panel of Fig. 8), while features such as those of the top panel of Fig. 10 can be explained as well. The latter can be comprehended on the basis of a superposition of a ghost state centered on the lossy side with a growing background, and of one (as in top left, or more as in the top right panel of Fig. 12) soliton(s) moving to the opposite direction and hence executing oscillations due to the absence of a ghost state to trap it. The above characteristics of the ghost states thus naturally lend themselves to the explanation of the static and dynamic phenomenology observed herein.

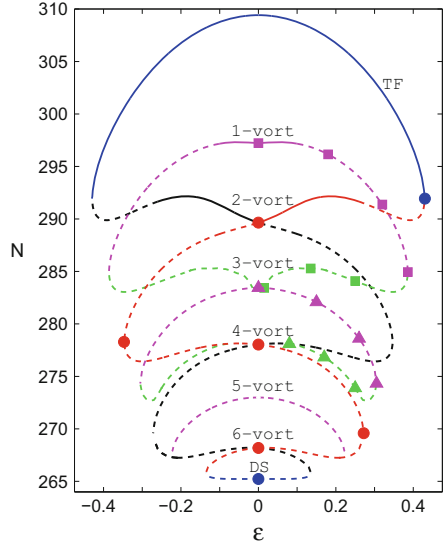
## 7 Symmetry Breaking and Nonlinear $\mathcal{PT}$ Phase Transitions in Two Dimensions

In order to consider the generalization of the ideas presented herein to higher dimensions, we now consider the case of a 2D  $\mathcal{PT}$ -symmetric potential ( $W(-x, -y) = -W(x, y)$ ) with

$$W(x, y) = \varepsilon(x + y)e^{-(x^2+y^2)/4}. \quad (41)$$

The configurations sustained in the 2D setting follow a similar symmetry breaking bifurcation scenario as in their 1D counterparts. However, the bifurcation structure is naturally expected to be more complex for the higher dimensional case. Figure 13 displays the bifurcation scenario for 2D solutions with and without topological charge for  $\Omega = 0.2$ . The bifurcation diagram includes the chargeless ground state (the TF background cloud), solutions bearing from one to six vortices, and the dark soliton stripe. Similar to the 1D case, the TF background is stable in all its domain of existence and collides, as  $\varepsilon$  increases, with an excited state (the two-vortex solution or vortex-dipole) in a blue-sky bifurcation at  $\varepsilon = \varepsilon_{\text{cr}}^{(2)}$ . However, in contrast to the 1D case where this collision occurs with the first excited state, in the 2D case the collision happens with the *second* excited state consisting of a vortex-dipole (a vortex pair with opposite charges). This is due to the fact that the TF background has no topological charge and, in turn, the vortex-dipole has also no net topological charge. This allows for the emergence of the vortex-dipole from a central dip on the TF background (see top panel of Fig. 14a) that becomes deeper as  $\varepsilon$  increases. This blue-sky bifurcation is depicted in Fig. 13 where the stable (center) TF branch (solid blue curve denoted by TF) collides with the unstable (saddle) vortex-dipole branch (red dashed curve denoted by 2-vort) at the 1D equivalent of the critical point  $\varepsilon = \varepsilon_{\text{cr}}^{(2)}$ .

**Fig. 13** Bifurcation diagram of stationary profiles in the 2D case. Stable and unstable branches, as determined by the corresponding BdG analysis, are depicted, respectively, with *solid* and *dashed* lines. The large symbols (*circles, squares and triangles*) denote the location in parameter space for the series of profiles depicted in Fig. 14. The parameter values are:  $\mu = 2$  and  $\Omega = 0.2$



It is possible to further follow the vortex-dipole branch by decreasing  $\varepsilon$  where we note that it regains stability for sufficiently smaller values of  $\varepsilon$  (see transition between the dashed and solid portions of the red line for the branch denoted by 2-vort). As this branch is followed further (from top to bottom in Fig. 13) a series of bifurcations arise where the vortices are drawn towards the edge of the cloud, a central dip deepens leading eventually to the emergence of a new vortex dipole in the middle of the cloud (namely, the emergence of a higher excited state). Therefore, the branches with *even* number of vortices are all inter-connected in this bifurcation scenario and only the TF branch and part of the vortex-dipole branch are stable. However, as more and more vortex pairs emerge, the extent of the cloud “saturates” as it can no longer support new vortex pairs and therefore is replaced by a dark soliton stripe (see dashed blue line denoted by DS in Fig. 13). This overall bifurcating scenario for even number of vortices is symmetric such that if  $\varepsilon \rightarrow -\varepsilon$  the solutions are just flipped by  $(x, y) \rightarrow (-x, -y)$ . Figure 14a depicts the density and phase profiles for different representatives along this branch.

Let us now describe the bifurcation scenario for *odd* number of vortices. The first excited state, corresponding to a single vortex, starts with a single vortex at the origin for  $\varepsilon = 0$  and it is stable for small values of  $\varepsilon$ . As in the 1D case, this first excited state suffers a SSB bifurcation at  $\varepsilon = \varepsilon_{\text{cr}}^{(1)}$  where it loses its stability. As  $\varepsilon$  is increased, the single vortex moves towards the periphery of the cloud and a dip at the center of the cloud deepens until a vortex dipole emerges at the center in the same way as new vortex-dipoles emerged for the branches with even number of vortices described above. This scenario connects, again through a blue-sky bifurcation, the one-vortex branch (magenta line denoted by 1-vort in Fig. 13) with the *asymmetric* three-vortex (+ - + vortex tripole) branch (green dashed

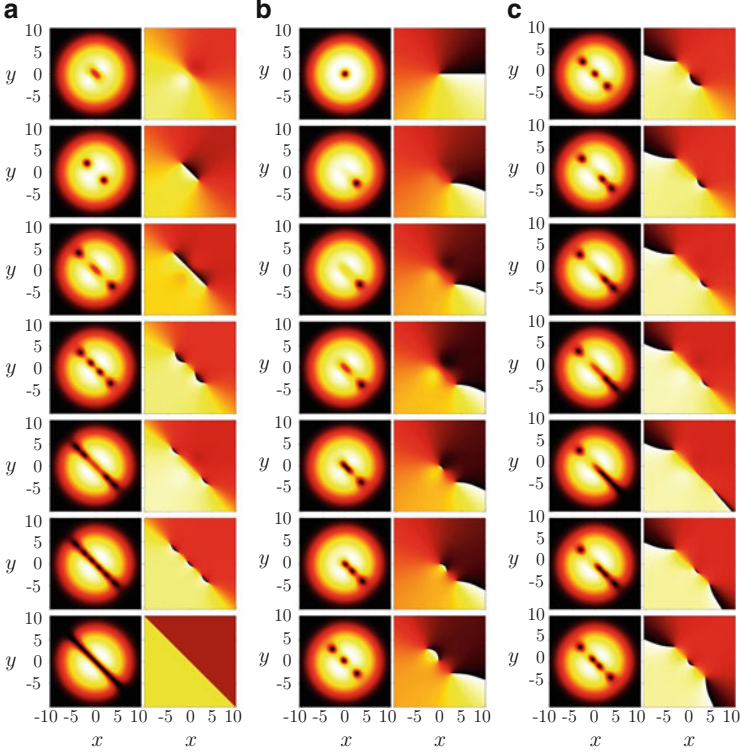


**Fig. 14** Stationary states in the 2D case corresponding to the main bifurcation branches in Fig. 13. The respective *left (right)* columns depict the density (phase) profiles of the solutions. **(a)** Profiles for the branch containing only even number of vortices corresponding to the circles in Fig. 13 (from top to bottom). **(b)** Profiles for the branch starting with a single vortex and connecting with three vortex branch corresponding to the squares in Fig. 13 (from top to bottom). **(c)** Profiles for the branch starting with three symmetric vortices and ending with four vortices corresponding to the triangles in Fig. 13 (from top to bottom). The parameter values are:  $\mu = 2$  and  $\Omega = 0.2$

line denoted by 3-vort in Fig. 13). The series of snapshots at the parameters depicted by the squares in Fig. 13 is depicted in Fig. 14b. It is nevertheless relevant to note that the blue-sky bifurcation for the single-triple vortex state (and more generally for any higher order pair of vortices) happens for values of  $\varepsilon$  lower than that of the bifurcation involving the TF ground state and the vortex-dipole state. Interestingly, although the structure of the relevant bifurcations is reminiscent of its one-dimensional analogue, there are also non-trivial differences, including the topological charge issue mentioned above, as well as the order in which the bifurcations occur (between more fundamental and more highly excited states) which is reversed. As it is evident from the figure, the asymmetric three-vortex branch eventually connects with the symmetric one for values of  $\varepsilon \rightarrow 0$ . A similar bifurcation occurs with the symmetric three-vortex branch, which becomes

asymmetric with a deepening dip at the center where a vortex pair emerges (at the same time that a vortex is lost at the periphery), connecting in this way with the four-vortex branch (see series of snapshots in panels Fig. 14c). As a relevant aside, let us also mention that all of the above true stationary states of the system (with real chemical potential or propagation constant) clearly form along the diagonal  $x + y = 0$  on which there is no gain or loss according to the prescription of Eq. (41).

It is important to mention that the precise structure of the bifurcation diagram depends on the values of the trap strength  $\Omega$  and the propagation constant  $\mu$ . In general terms, for weaker  $\Omega$  and/or larger  $\mu$  the spatial extent of the TF background will be larger and thus allowing for a longer bifurcating chain of higher-order vortex states (before all the vortices finally merge into a dark soliton stripe). Nonetheless, the displayed SSB instabilities and the nonlinear  $\mathcal{PT}$  phase transition involving the cascade of blue-sky bifurcations appear to be universal in confining  $\mathcal{PT}$ -symmetric potentials as considered herein.

Let us now describe the dynamics of the unstable steady states described in the above bifurcation scenario. We first start by describing the unstable dynamics of single vortex states. In this case, in analogy with the 1D case, single vortex states tend to migrate towards the lossy side of the potential. This tendency is depicted by the series of density snapshots in Fig. 15a, b where *unstable* single vortex states for  $\varepsilon = 0.2$  and  $\varepsilon = 0.35$ , respectively, migrate to different positions within the lossy side. This phenomenology can be very clearly understood on the basis of our ghost state interpretation. Once again, ghost states are present here corresponding to a unique shift of the vortex center to a location such that  $x_0 + y_0 < 0$ . This state is associated with  $\mu_I > 0$ , due to the fact that  $\iint W(x, y) |u(x, y)|^2 dx dy > 0$  and hence leads to growth of the amplitude and width of the condensate, a trait which can be clearly observed in the relevant panels. It is also important to mention that the stable single vortex, close to where it loses stability, is only weakly stable and can be ‘kicked out’ by a relatively small perturbation towards the lossy side. This scenario is depicted in Fig. 15c where the *stable* single vortex configuration for  $\varepsilon = 0.1$  is perturbed by applying a small rotation of  $5^\circ$ . Although the rotation is very small and that the unperturbed configuration is stable, we note that the vortex eventually migrates (after a long transient, see that time in the series of snapshots runs to  $t = 3,000$ ) towards the lossy side. Further numerics shows that angles larger than  $4^\circ$  display the same dynamics while smaller angles correspond to the single vortex returning periodically towards its original position (see for example the periodic orbit depicted in Fig. 15d where the stable vortex is initially rotated by  $4^\circ$ ). To complement the snapshots for the evolution of the different configurations, we depict in Fig. 16 the evolution of the corresponding power  $N(t) = \iint |u(x, y, t)|^2 dx dy$  and the total angular momentum  $L_z(t) = -i \iint u^* \partial_\theta u dx dy$ . As it may be observed from panel (a), the migration of the unstable vortices towards the lossy side does not initially (see flat portion in the figures for relatively short times) affect significantly the total power, nor the angular momentum. However, once the vortex settles in the lossy side and the background starts growing the power and angular momentum increase rapidly. In contrast, as depicted in Fig. 16b, for the case of a stable vortex slightly perturbed

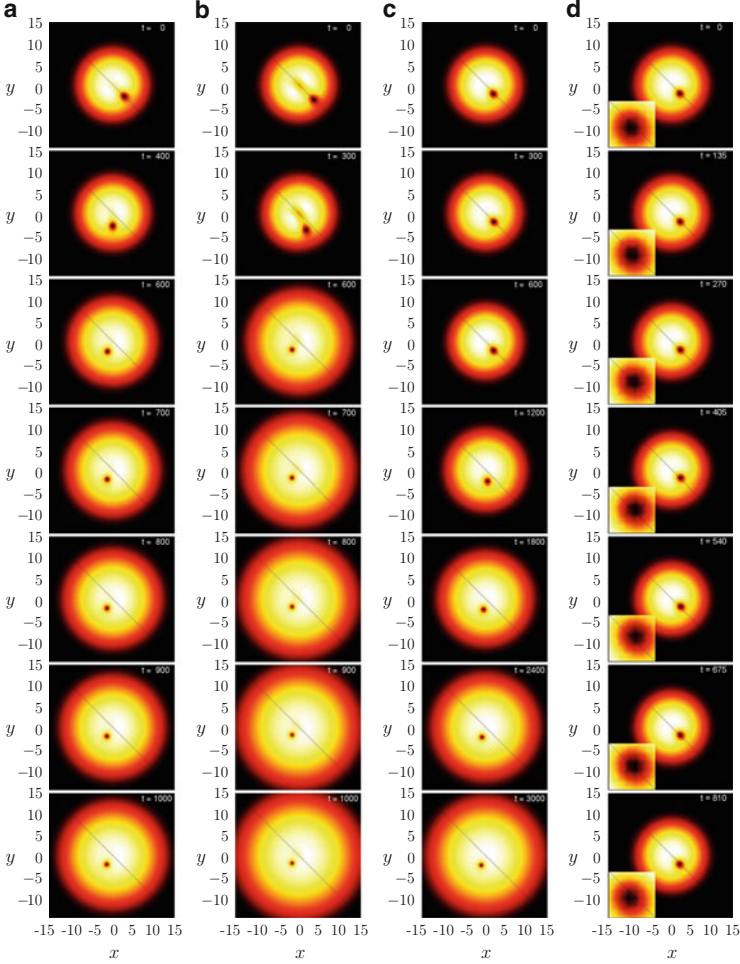


**Fig. 15** Dynamics of unstable steady states in the 2D case. All panels depict the density profiles at the times indicated for  $\mu = 2$  and  $\Omega = 0.2$ . The *thin diagonal line* in all panels depicts the border between the loss and gain sides of  $W(x, y)$ . **(a and b)** Unstable single vortex state for  $\varepsilon = 0.2$  and  $\varepsilon = 0.35$ , respectively. **(c)** Stable single vortex configuration for  $\varepsilon = 0.1$  perturbed by a small rotation of  $5^\circ$ . **(d)** Stable single vortex configuration for  $\varepsilon = 0.1$  perturbed by a small rotation of  $4^\circ$  performs a periodic oscillation around its original position (a single period is shown, see zoom in the *inset*)

from its original location the power and angular momentum perform oscillations corresponding to the oscillations of the perturbed vortex observed in Fig. 15d. Another interesting example is that of panel (e), corresponding to Figs. 18c, d and 19a, b below. Notice that a fundamental difference in this case (in analogy to what we observed in the 1D setting) is the fact that the vortices do not settle on the lossy side (in the form of ghost states) but rather oscillate between the gain and the loss

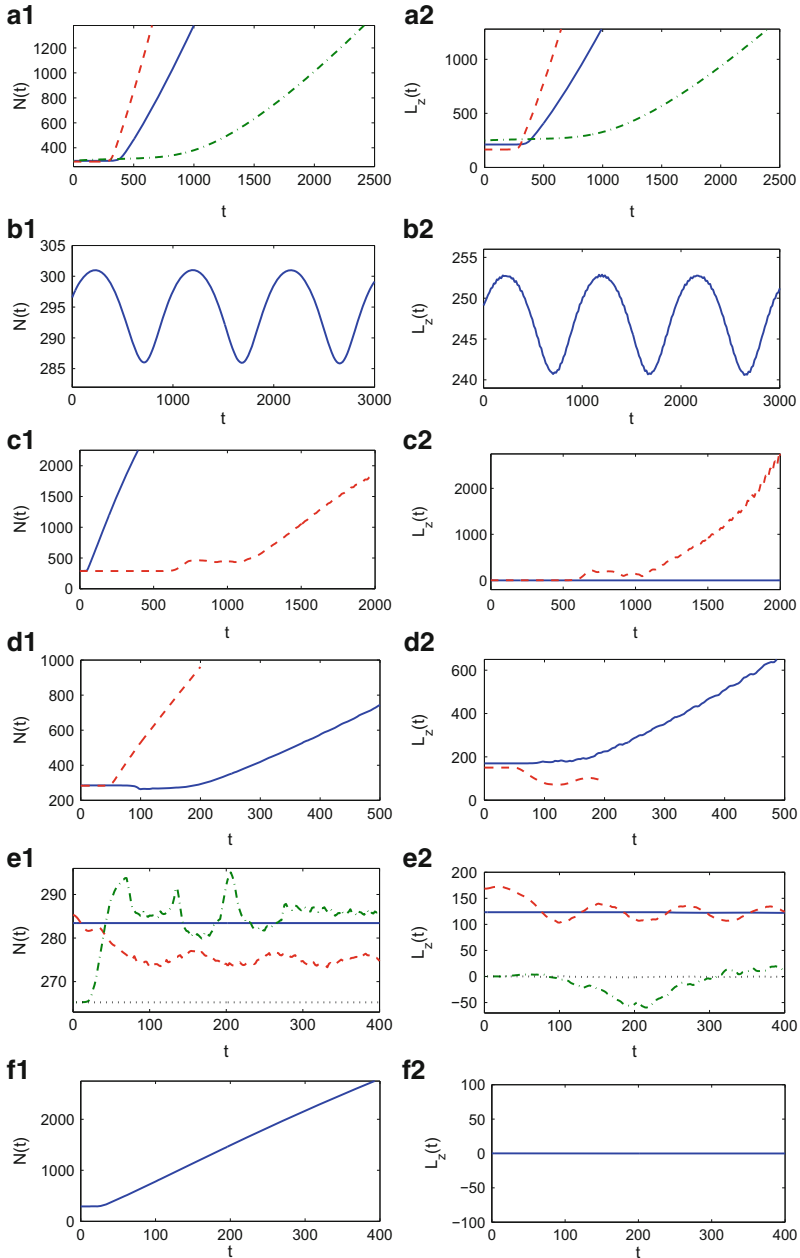
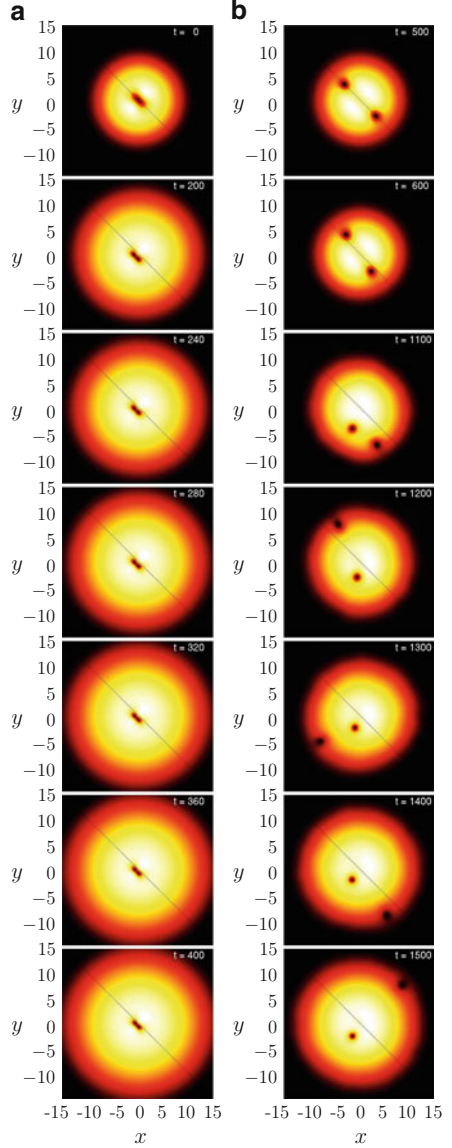


**Fig. 16** Evolution of the power  $N(t)$  (left column) and the angular momentum  $L_z(t)$  (right column) corresponding to the dynamics for the following configurations: **(a)** Fig. 15a–c depicted with solid (blue), dashed (red), and dash-dotted (green) lines, respectively. **(b)** Fig. 15d. **(c)** Fig. 17a, b depicted with solid (blue) and dashed (red) lines, respectively. **(d)** Fig. 18a, b depicted with solid (blue) and dashed (red) lines, respectively. **(e)** Figs. 18c, d and 19a, b depicted with solid (blue), dashed (red), dash-dotted (green), and dotted (black) lines, respectively. **(f)** Fig. 18c

**Fig. 17** Same as in Fig. 15 for the following two-vortex scenarios. **(a)** Unstable tight vortex-dipole state belonging to the branch directly connecting with the TF cloud (depicted by the *red dashed line* denoted by 2-vort in Fig. 13) for  $\varepsilon = 0.4$ . **(b)** Unstable, well separated, two-vortex state belonging to the branch connecting with the four-vortex branch (depicted by the *black dashed line* denoted by 2-vort in Fig. 13) for  $\varepsilon = 0.2$



side. Importantly, note that these two examples each contain a Hamiltonian case (Figs. 18c and 19b), where the energy and angular momentum are conserved and a gain-loss one where the evolution is oscillatory, yet does not lead to indefinite growth as in other examples of Fig. 16.

Let us now describe the evolution of unstable vortex-dipoles. In Fig. 17a we depict the evolution of a *tight* vortex-dipole close to the parameter values where it is created (i.e., in the dip at the center of the cloud). As the figure shows, the

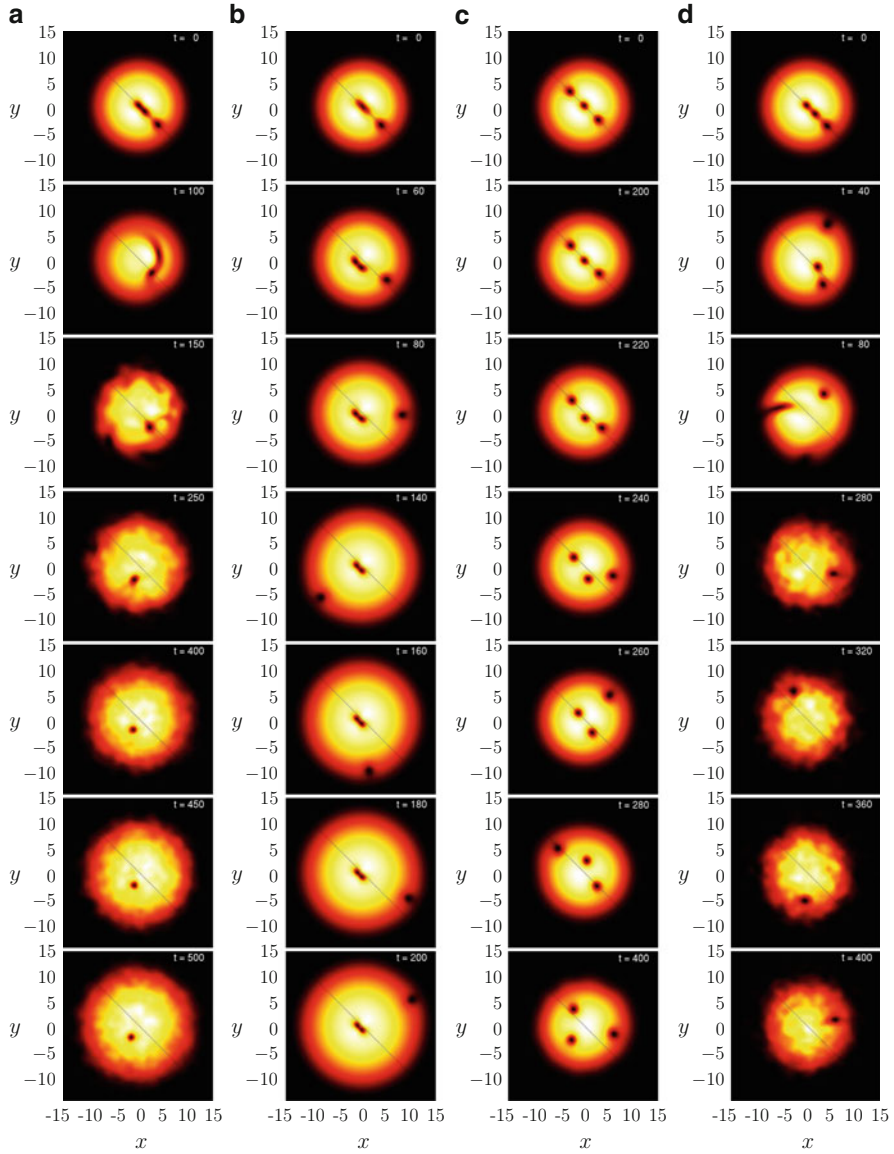


**Fig. 18** Same as in Fig. 15 for the following three-vortex scenarios. (a and b) Unstable asymmetric three-vortex states (depicted by the *green dashed line* denoted by 3-vort in Fig. 13) for  $\varepsilon = 0.2$  and  $\varepsilon = 0.35$ , respectively. (c) Unstable symmetric three-vortex state for  $\varepsilon = 0$ . (d) Unstable asymmetric three-vortex state (depicted by the *green dashed line* denoted by 3-vort in Fig. 13) for  $\varepsilon = 0.1$

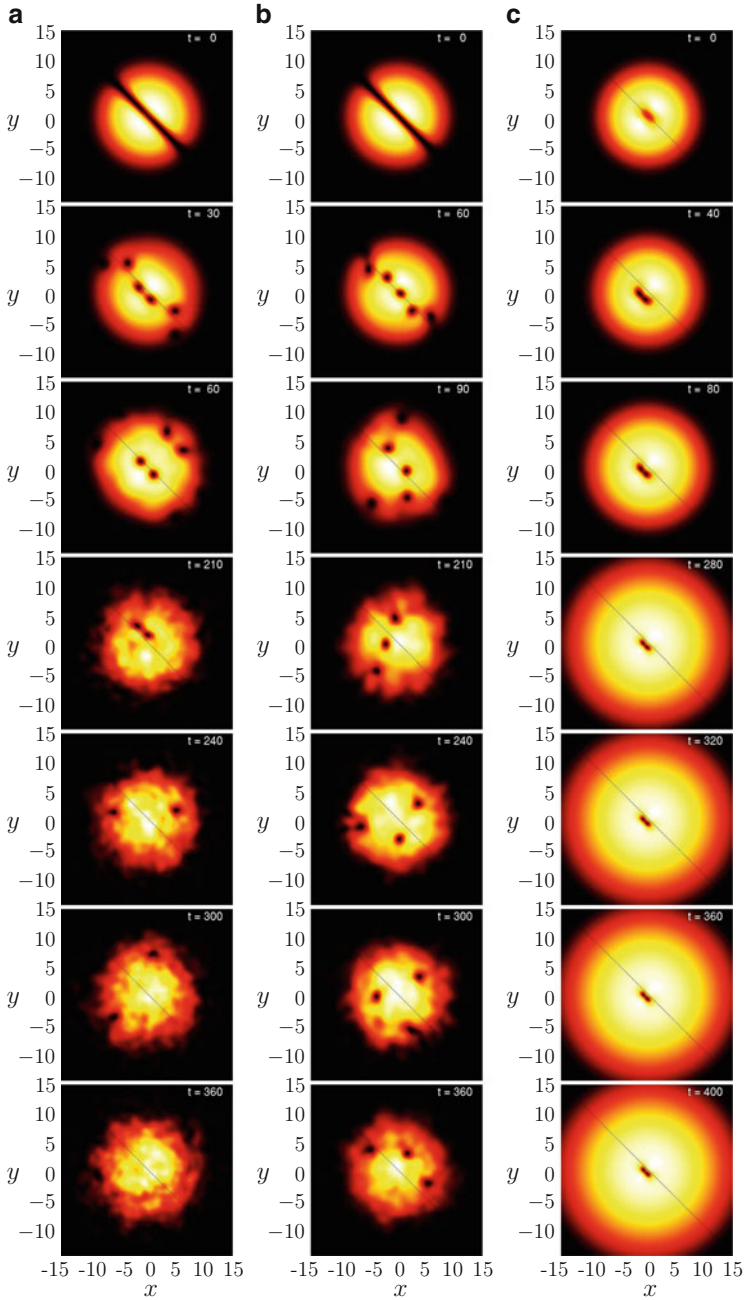


**Fig. 19** Same as in Fig. 15 for the following scenarios. (a and b) Unstable dark soliton stripes (depicted by the lowest blue dashed line denoted by DS in Fig. 13) for  $\varepsilon = 0.1$  and  $\varepsilon = 0$ , respectively. (c) Thomas-Fermi (ground) state obtained for  $\varepsilon = 0.4$  and let to evolve for  $\varepsilon = 0.43$

tight vortex-dipole undergoes a small excursion into the lossy side and, as time progresses, it re-approaches to the center of the cloud at the same time that the cloud grows (as in the 1D case). Clearly the relevant interpretation here involves the existence of a ghost state which attracts the dynamics and contains both vortex members of the dipole on the lossy side of the system. In this case, as it is depicted by the solid (blue) line in Fig. 16c, the power increases but the angular momentum remains equal to zero since the vortices are of opposite charge. In Fig. 17b we depict the dynamics arising from a *well separated* unstable vortex-dipole state. We typically observe that, for a well separated unstable vortex dipole, one vortex is trapped at a suitable location within the lossy side while the other vortex circles around slowly approaching the periphery of the cloud where it is finally absorbed. This is in a number of ways tantamount to the two-soliton dynamics that we explored in Fig. 10. Generally, it is clear that the three possible dynamical scenario for the vortices constituting the dipole and involving ghost states here are that either both vortices transition to the lossy side (Fig. 17a), or one (Fig. 17b) or none (not shown here).

Let us now briefly describe some typical evolution examples for higher order unstable states. In particular, let us start by discussing the three-vortex states. Figure 18a depicts the evolution of an unstable asymmetric 3-vortex profile. In this case, the outer vortex migrates towards the attracting basin within the lossy side while the remaining vortex-dipole gets violently ejected and the two vortices annihilate each other. This again confirms the dynamical relevance of the single-vortex corresponding ghost state. Another possible scenario for the 3-vortex configuration is depicted in Fig. 18b where this time the central vortex-dipole slowly migrates towards the lossy side and slowly re-approaches the center of the trap as time progresses while the outer vortex performs large excursions around the periphery of the cloud where it is eventually absorbed. In this setting, we observe once again the dynamics of a vortex-dipole ghost state (with the background in this, as well as in the previous example featuring the analyzed growth and concurrent spreading). For contrasting purposes, we depict in Fig. 18c the dynamics of an unstable *symmetric* three-vortex state for  $\varepsilon = 0$ . In this case, the external potential is conservative and the motion of the three vortices is Hamiltonian and thus, typically, the three vortices will remain orbiting inside the cloud for very long times. Nevertheless, notice in the latter case the well established (and generic) instability of the Hamiltonian vortex tripole which leads to its break-up into a vortex dipole and a single vortex [43, 44]. Finally, in Fig. 18d we depict the evolution of another unstable asymmetric state. In this case it can be observed that two vortices annihilate each other and the third does not get absorbed by the lossy side as in Fig. 18a, but it performs large oscillations close to the periphery of the cloud where it is finally absorbed. The precession of this vortex due to its initial placement within the gain side suggests a direct analogy of this case (and after the dipole annihilation) with the top left panel of Fig. 8.

Finally, we briefly explore the dynamics of unstable dark soliton stripes. Dark soliton stripes are known to be unstable in the Hamiltonian case ( $\varepsilon = 0$ ) due to the so-called snaking instability [45, 46] (although they can be rendered stable by a very tightly confining trap [47] or a wall-like external potential [48]). Figure 19a

depicts the typical evolution of an unstable dark soliton stripe solution in the non-Hamiltonian ( $\mathcal{PT}$ -symmetric) case. In this case, the dark soliton stripe decays into a chain of alternating charge vortices induced by the snaking instability and their long term behavior includes annihilation and large oscillations where they get eventually absorbed at the periphery of the cloud leaving behind a highly perturbed (chargeless) Thomas-Fermi ground state. In contrast, as depicted in Fig. 19b, for the Hamiltonian case of  $\varepsilon = 0$ , most of the vortices that formed from the snaking instability remain interacting for long times (i.e., the latter are more likely to survive here, analogously to what we also saw for the tripole case above). Finally, in Fig. 19c we depict the evolution when starting with a TF cloud for  $\varepsilon$  past the critical value of existence of the stationary TF cloud. In this example, we compute the stationary (stable), chargeless, steady TF profile for  $\varepsilon = 0.4$  and run it with  $\varepsilon = 0.43$  (i.e., past the blue-sky bifurcation between the TF cloud and the vortex dipole states). We observe in this simulation that the central dip of the TF (which contains no charge) rapidly gets converted into a tight vortex-dipole state which does a small excursion towards the lossy side (very similar to the dynamics of the unstable tight vortex-dipole profile of Fig. 17a), clearly suggesting the persistence and dynamical selection of the corresponding vortex-dipole ghost state. This behavior is akin to what we observed in 1D for values of  $\varepsilon$  past  $\varepsilon_{\text{cr}}^{(2)}$  (the dark soliton ‘sprinkler’ case) where excited states with topological charge are dynamically created from chargeless configurations. Hence, the two-dimensional setting may be used as a “vortex sprinkler”.

## 8 Conclusions

In the present work, we offered a basic, yet reasonably self-contained view on the fundamental modifications that the phenomenology of nonlinear entities sustains in the presence of  $\mathcal{PT}$ -symmetric confining potentials (although the case where there is no real potential was also touched upon as well). The prototypical among the observed features of such systems were found to be the emergence of symmetry breaking bifurcations that destabilize single, triple, five, etc. soliton states in one dimension and similarly one- or two- or higher vortex states in two-dimensions. The second important and unexpected feature was the emergence of a nonlinear analogue of the  $\mathcal{PT}$ -phase-transition, whereby e.g. the ground and first excited, the second and third excited, the fourth and fifth excited state and so on (in 1D) are led to pairwise collisions and blue-sky bifurcations. Generalizations of these effects which, however, properly respect the topological nature of the states (e.g. the zero-vortex with the vortex dipole, the single vortex with the vortex tripole etc.) are found to arise in the two-dimensional setting. In addition, the pitchfork nature of the symmetry-breaking bifurcation was illustrated through the examination of the so-called ghost states and the proof, not only of their genuinely complex eigenvalue parameter, but also of their direct relevance for the dynamics of the full problem, despite the fact that they do not constitute exact solutions thereof (but rather only

solutions of the static problem). The dynamical evolution of unstable soliton and vortex states was examined for all the identified instabilities, revealing a wealth of possibilities involving ghost states, soliton/vortex sprinklers, and oscillations between the loss and gain sides.

It would be interesting to offer a detailed map of the ghost states of the system. Here, we have illustrated their existence and observed many of their dynamical implications, yet a systematic characterization of their emergence (and perhaps the more challenging understanding of their basins of attraction) certainly merits further examination. On the other hand, a feature that has been examined in some detail in the context of  $\mathcal{PT}$ -symmetric linear problems which is, arguably, worthwhile to consider here concerns the analytic continuation of the states past the point of the  $\mathcal{PT}$ -phase-transition. This was already touched upon in the nonlinear realm for double well potentials in the work of Refs. [35–38], but it would be relevant to offer a definitive view of such analytically continued states for general potentials. Finally, a canonical set of investigations which is still missing concerns the effects of such potentials in three-dimensional continuum or one- and higher-dimensional (infinite) lattice contexts. These topics will be pursued in future publications.

**Acknowledgements** V.A. gratefully acknowledges support from the A.G. Leventis Foundation. P.G.K. gratefully acknowledges support from the National Science Foundation under grants DMS-0806762 and CMMI-1000337, as well as from the Alexander von Humboldt Foundation, the Alexander S. Onassis Public Benefit Foundation and the Binational Science Foundation. The work of D.J.F. was partially supported by the Special Account for Research Grants of the University of Athens. R.C.G. gratefully acknowledges support from the National Science Foundation under grant DMS-0806762.

## References

1. C.M. Bender, S. Boettcher, Phys. Rev. Lett. **80**, 5243 (1998)
2. C.M. Bender, S. Boettcher, P.N. Meisinger, J. Math. Phys. **40**, 2201 (1999); C.M. Bender, Rep. Prog. Phys. **70**, 947 (2007)
3. A. Ruschhaupt, F. Delgado, J.G. Muga, J. Phys. A: Math. Gen. **38**, L171 (2005)
4. Y. Chen, A.W. Snyder, D.N. Payne, IEEE J. Quantum Electron. **28** 239 (1992)
5. Z.H. Musslimani, K.G. Makris, R. El-Ganainy, D.N. Christodoulides, Phys. Rev. Lett. **100**, 030402 (2008)
6. K.G. Makris, R. El-Ganainy, D.N. Christodoulides, Z.H. Musslimani, Phys. Rev. A **81**, 063807 (2010)
7. A. Guo, G.J. Salamo, D. Duchesne, R. Morandotti, M. Volatier-Ravat, V. Aimez, G.A. Siviloglou, D.N. Christodoulides, Phys. Rev. Lett. **103**, 093902 (2009)
8. C.E. Rüter, K.G. Makris, R. El-Ganainy, D.N. Christodoulides, M. Segev, and D. Kip, Nat. Phys. **6**, 192 (2010)
9. J. Schindler, A. Li, M.C. Zheng, F.M. Ellis, T. Kottos, Phys. Rev. A **84**, 040101 (2011)
10. H. Ramezani, T. Kottos, R. El-Ganainy, and D.N. Christodoulides, Phys. Rev. A **82**, 043803 (2010)
11. A.A. Sukhorukov, Z. Xu, Yu.S. Kivshar, Phys. Rev. A **82**, 043818 (2010)
12. M.C. Zheng, D.N. Christodoulides, R. Fleischmann, T. Kottos, Phys. Rev. A **82**, 010103(R) (2010)

13. E.M. Graefe, H.J. Korsch, A.E. Niederle, Phys. Rev. Lett. **101**, 150408 (2008)
14. E.M. Graefe, H.J. Korsch, A.E. Niederle, Phys. Rev. A **82**, 013629 (2010)
15. Z. Lin, H. Ramezani, T. Eichelkraut, T. Kottos, H. Cao, D.N. Christodoulides, Phys. Rev. Lett. **106**, 213901 (2011)
16. K. Li, P.G. Kevrekidis, Phys. Rev. E **83**, 066608 (2011)
17. S.V. Dmitriev, S.V. Suchkov, A.A. Sukhorukov, Yu.S. Kivshar, Phys. Rev. A **84**, 013833 (2011)
18. S.V. Suchkov, B.A. Malomed, S.V. Dmitriev, Yu.S. Kivshar, Phys. Rev. E **84**, 046609 (2011)
19. R. Driben, B.A. Malomed, Opt. Lett. **36**, 4323 (2011)
20. R. Driben, B.A. Malomed, Europhys. Lett. **96**, 51001 (2011)
21. F.Kh. Abdullaev, V.V. Konotop, M. Ögren, M.P. Sørensen, Opt. Lett. **36**, 4566 (2011)
22. N.V. Alexeeva, I.V. Barashenkov, A.A. Sukhorukov, Yu.S. Kivshar, Phys. Rev. A **85**, 063837 (2012)
23. A.A. Sukhorukov, S.V. Dmitriev, Yu.S. Kivshar, Opt. Lett. **37**, 2148 (2012)
24. A.E. Miroshnichenko, B.A. Malomed, Yu.S. Kivshar, Phys. Rev. A **84**, 012123 (2011)
25. F. Kh. Abdullaev, Y.V. Kartashov, V.V. Konotop, D.A. Zezyulin, Phys. Rev. A **83**, 041805 (2011)
26. D.A. Zezyulin, Y.V. Kartashov, V.V. Konotop, Europhys. Lett. **96**, 64003 (2011)
27. D.A. Zezyulin, V.V. Konotop, Phys. Rev. A **85**, 043840 (2012)
28. H.G. Li, Z.W. Shi, X.J. Jiang, X. Zhu, Opt. Lett. **36**, 3290 (2011)
29. V. Achilleos, P.G. Kevrekidis, D.J. Frantzeskakis, R. Carretero-González, Phys. Rev. A **86**, 013808 (2012)
30. P.G. Kevrekidis, D.J. Frantzeskakis, R. Carretero-González, *Emergent Nonlinear Phenomena in Bose-Einstein Condensates: Theory and Experiment* (Springer, Heidelberg, 2008)
31. Yu.S. Kivshar, G.P. Agrawal, *Optical solitons: from fibers to photonic crystals* (Academic, San Diego, 2003)
32. S. Klaiman, U. Günther, N. Moiseyev, Phys. Rev. Lett. **101**, 080402 (2008)
33. P.Würtz, T. Langen, T. Gericke, A. Koglbauer, H. Ott, Phys. Rev. Lett. **103**, 080404 (2009)
34. M. Hiller, T. Kottos, A. Ossipov, Phys. Rev. A **73**, 063625 (2006)
35. H. Cartarius, G. Wunner, Phys. Rev. A **86**, 013612 (2012); H. Cartarius, D. Haag, D. Dast, G. Wunner, J. Phys. A: Math. Theor. **45**, 444008 (2012)
36. E.-M. Graefe, J. Phys. A: Math. Theor. **45**, 444015 (2012)
37. D. Dast, D. Haag, H. Cartarius, G. Wunner, R. Eichler, J. Main, Fortschr. Phys. (in press). doi:10.1002/prop.201200080
38. A.S. Rodrigues, K. Li, V. Achilleos, P.G. Kevrekidis, D.J. Frantzeskakis, C.M. Bender, Romanian Reports in Physics **65**, 5 (2013). arXiv:1207.1066
39. D.J. Frantzeskakis, J. Phys. A: Math. Theor. **43**, 213001 (2010)
40. Yu.S. Kivshar, B. Luther-Davies, Phys. Rep. **298**, 81 (1998)
41. G. Theocharis, P.G. Kevrekidis, M.K. Oberthaler, D.J. Frantzeskakis, Phys. Rev. A **76**, 045601 (2007); A. Weller, J.P. Ronzheimer, C. Gross, J. Esteve, M.K. Oberthaler, D.J. Frantzeskakis, G. Theocharis, P.G. Kevrekidis, Phys. Rev. Lett. **101**, 130401 (2008); G. Theocharis, A. Weller, J.P. Ronzheimer, C. Gross, M.K. Oberthaler, P.G. Kevrekidis, D.J. Frantzeskakis, Phys. Rev. A **81**, 063604 (2010)
42. P.G. Kevrekidis, D.J. Frantzeskakis, Discr. Cont. Dyn. Sys. S **4**, 1199 (2011)
43. S. Middelkamp, P.G. Kevrekidis, D.J. Frantzeskakis, R. Carretero-González, P. Schmelcher, Phys. Rev. A **82**, 013646 (2010)
44. J. Stockhofe, S. Middelkamp, P.G. Kevrekidis, P. Schmelcher, EPL **93**, 20008 (2011)
45. E.A. Kuznetsov, J.J. Rasmussen, Phys. Rev. E **51**, 4479 (1995)
46. D.E. Pelinovsky, Yu.A. Stepanyants, Yu.S. Kivshar, Phys. Rev. E **51**, 5016 (1995)
47. P.G. Kevrekidis, G. Theocharis, D.J. Frantzeskakis, A. Trombettoni, Phys. Rev. A **70**, 023602 (2004)
48. Manjun Ma, R. Carretero-González, P.G. Kevrekidis, D.J. Frantzeskakis, B.A. Malomed, Phys. Rev. A **82**, 023621 (2010)